JOURNAL OF AIRCRAFT
Vol. 48, No. 3, May–June 2011

# Influence of Blade Aerodynamic Model on Prediction of Helicopter Rotor Aeroacoustic Signatures

Mary E. Kelly*
*University of Glasgow, Glasgow, Scotland G12 8QQ, United Kingdom*
and
Richard E. Brown†
*University of Strathclyde, Glasgow, Scotland G1 1XJ, United Kingdom*

DOI: 10.2514/1.C031232

**Brown's vorticity transport model has been used to investigate how the local blade aerodynamic model influences the quality of the prediction of the high-frequency airloads associated with blade–vortex interactions, and thus the accuracy with which the acoustic signature of a helicopter rotor can be predicted. The vorticity transport model can accurately resolve the structure of the wake of the rotor and allows significant flexibility in the way that the blade loading can be represented. The Second Higher-Harmonic Control Aeroacoustics Rotor Test was initiated to provide experimental insight into the acoustic signature of a rotor in cases of strong blade–vortex interaction. Predictions of two models for the local blade aerodynamics are compared with the test data. A marked improvement in accuracy of the predicted high-frequency airloads and acoustic signature is obtained when a lifting-chord model for the blade aerodynamics is used instead of a lifting-line-type approach. Errors in the amplitude and phase of the acoustic peaks are reduced, and the quality of the prediction is affected to a lesser extent by the computational resolution of the wake, with the lifting-chord model producing the best representation of the distribution of sound pressure below the rotor.**

## Nomenclature

| | | |
|---|---|---|
| $a_{ij}$ | = | interpolation coefficients |
| $b$ | = | blade semichord |
| $c$ | = | blade chord, $2b$ |
| $C_N$ | = | section normal force coefficient |
| $C_T$ | = | rotor thrust coefficient, $T/\rho A(\Omega R)^2$ |
| $f$ | = | reverse flow parameter |
| $F_j(\psi)$ | = | azimuthal interpolation functions |
| $K$ | = | coefficient of integration |
| $M$ | = | Mach number, $U_\infty/a$ |
| $N_a$ | = | number of azimuthal interpolation functions |
| $N_r$ | = | number of radial interpolation functions |
| $P_i(r)$ | = | radial interpolation functions |
| $R$ | = | rotor radius |
| $r$ | = | blade spanwise coordinate scaled by $R$ |
| $S$ | = | local vorticity source |
| $t$ | = | time |
| $\boldsymbol{u}$ | = | flow velocity vector |
| $U_\infty$ | = | magnitude of freestream velocity |
| $w$ | = | blade velocity relative to background flow |
| $X$ | = | rotor streamwise coordinate |
| $x$ | = | aerofoil chordwise coordinate, $b\cos\varphi$ |
| $Y$ | = | rotor lateral coordinate |
| $y_{\mathrm{el}}$ | = | elastic lag motion |
| $Z$ | = | rotor vertical coordinate |
| $z_{\mathrm{el}}$ | = | elastic flap motion |
| $\Gamma$ | = | total bound circulation |
| $\lambda$ | = | velocity due to vorticity in flow |
| $\nu$ | = | viscosity of fluid |
| $\theta_{\mathrm{el}}$ | = | elastic blade torsion |
| $\rho$ | = | density of fluid |
| $\tau$ | = | unit vector parallel to blade downwind edge |
| $\varphi$ | = | Glauert variable |
| $\psi$ | = | azimuth angle |
| $\omega$ | = | vorticity in flow |

Received 8 September 2010; revision received 2 February 2011; accepted for publication 3 February 2011. 

*Department of Aerospace Engineering.
†Department of Mechanical Engineering.

## I. Introduction

THE aerodynamic environment in which a rotorcraft operates is dominated by the strong vortical structures that are generated by the rotating blades of its rotors. The interaction between these vortices and the various structural components of the aircraft accounts for many of the design problems that rotorcraft encounter. In particular, the localized aerodynamic interactions between the rotor blades and the vortices that they produce, known as blade–vortex interactions (BVIs), result in highly impulsive loads along the blade span and are a significant source of noise and vibration. The intensity and directivity of the noise generated by a helicopter is of considerable importance for both civilian and military applications, as strict certification and community noise constraints often apply. Such requirements have led the rotorcraft community to investigate the sources of noise associated with helicopters in flight with the aim of significantly reducing current noise levels.

To accurately predict the noise produced by a particular design of aircraft, it is essential to first accurately determine the position, amplitude, and strength of the BVI-induced loading perturbations on the rotor blades. This process requires the accurate determination of both the position and strength of the vortical structures in the wake and the correct position and deformation of the rotor blades. The complexity of the rotor wake and the strong mutual dependence of the aerodynamics and structural dynamics of the blades render accurate prediction of the BVI-related blade airloads a particularly challenging task. A tool that can accurately predict the high-frequency components of the blade loading, particularly those that are responsible for the rather objectionable acoustic characteristics of the helicopter under certain flight conditions, would be of significant benefit to the designers of modern rotorcraft in the drive to reduce noise.

The Higher-Harmonic Control Aeroacoustics Rotor Test (HART) program [1–4] was initiated to provide experimental insight into the structure of the rotor wake and the effect of the wake on the aerodynamic loading on the rotor blades and, thus, on the acoustic signature of the rotor. The rotor that was used in this program was a

scaled model of that used on the Bo105 helicopter. The experiment was designed specifically to replicate a descending flight condition in which the loading on the rotor was known to contain significant high-frequency content due to the presence of BVIs.

Computational fluid dynamics (CFD) calculations of the flow around the entire rotorcraft, or even just the rotor, are extremely challenging. Nevertheless, recent advances in coupling rotorcraft computational structural dynamic (CSD) analyses to rotorcraft CFD have demonstrated significant progress in accurately predicting the rotor blade motion and capturing the associated blade airloads. Boyd [5], Lim et al. [6], and Lim and Strawn [7] showed encouraging results in comparison with experimental data for their prediction of the BVI-induced airloads from the second HART experiment (HART II), for instance. For most CFD methods, the numerical dissipation that is inherent in the approach necessitates very high grid densities to maintain the fidelity of the wake, particularly if the structure of the wake is to be resolved to a level where the high-frequency character of the BVI-generated airloads can be captured. At present, this invariably results in solutions that are grid dependent, given the prohibitive computational cost of rotor calculations on grids that are sufficiently fine to resolve the detailed structure of the wake.

There is a drive within the industry, particularly in the context of rotor design, to develop methods that can achieve high-fidelity resolutions, but at a much reduced computational cost when compared with CFD calculations of full helicopter configurations. One approach is via the so-called comprehensive code, which couples structural and aerodynamics analyses to a flight dynamics model. Such an approach often uses lifting-line or lifting-surface types of aerodynamic models to provide blade airload information and a prescribed- or free-wake approach to portray the dynamics of the wake system. Often, though, comprehensive analyses require empirical corrections to accurately portray the unsteady aerodynamics within the flowfield, and additional considerations are required to account for compressibility effects and stall. Lifting-line or lifting-surface types of aerodynamic models are relatively simple and easy to implement, but the physical accuracy of their response to the dynamics of the wake, especially if this is based on a prescribed- or free-wake approach, can be called into question, especially in terms of resolving the detail of the close blade–wake encounters associated with BVI. It is often not clear whether discrepancies in the wake model or in the blade aerodynamic model that lies at the source of the wake are responsible for the deficiencies in prediction of the BVI-induced loads that appear to be characteristic of this type of approach.

The vorticity transport model (VTM) is a comprehensive rotorcraft model in which the evolution of the wake is based on a time-dependent vorticity–velocity formulation of the Navier–Stokes equations, solved computationally on a structured grid system surrounding the rotor. This approach has been shown to yield a very accurate representation of the vortical structures within the wake of the rotor, yet it offers significant flexibility in the way that the source of vorticity into the wake can be generated. For instance, a simple lifting-line model for the blade aerodynamics can be used or a full primitive-variable CFD calculation of the blade flow can be embedded in the calculation [8]. This flexibility makes the VTM ideal for studying the effect of the blade aerodynamic model on the fidelity of the prediction of the high-frequency BVI-induced loads on the rotor.

The VTM framework has been used previously to predict the geometry of the wake system and the resultant rotor blade loading for the HART II rotor, using a lifting-line model for the blade aerodynamics [9,10] and in comparison with a lifting-chord model [11] based on unsteady thin aerofoil theory. These earlier investigations suggested that accurate prediction of the high-harmonic BVI-induced component of the airloads on the rotor is greatly influenced by the accuracy to which the wake geometry can be represented. Moreover, the high-frequency BVI-induced component of the loading is very sensitive to the cell size that is used in the computations when a lifting-line model is used to represent the aerodynamic environment of the rotor blades. Sensitivity to the computational resolution that is used is reduced markedly when a lifting-chord model is used in place of the lifting-line approach. Nevertheless, comparisons of the predicted wake structure and the trajectory of the vortices as they pass through the rotor disk have shown excellent agreement with the vortex core positions as measured during the HART II experiment, regardless of the aerodynamic model that is used [9,10].

The work presented in [11] focused on the aerodynamic issues involved in predicting the blade airloads and the rotor wake structure in regimes dominated by strong BVI. In particular, the effect of the fidelity of the local model for the blade aerodynamics on the quality of the BVI-airload predictions was investigated. This paper extends that work by comparing the measured acoustic signature of the HART II rotor with that calculated from the airloads predicted by Brown's VTM when coupled to the two different approaches to modeling the local aerodynamics of the blades. This work aims to correlate the various salient features in the acoustic signal produced by the rotor to the specific features within the blade loading, and thus to refine our understanding of how the predictions of the acoustic signature of the rotor are affected by the fidelity of the model that is used to predict its aerodynamic loading.

## II. Rotor Model

### A. Second Higher-Harmonic Aeroacoustics Rotor Test

The model rotor used in the HART II test was based on that of the Bo105 main rotor. The rotor had four blades and was scaled both geometrically and aeroelastically to 40% of the full rotor size, giving a radius of 2 m and a chord of 0.121 m. The rotor blades had a NACA23012 aerofoil with the trailing edge modified to form a 5.4 mm (4.46% chord) tab. The blades were rectangular with square tips, and they incorporated $-8^\circ$ of linear twist and a precone angle of $2.5^\circ$.

The rotor was operated at an advance ratio of 0.15 during the test, with a rotor shaft inclination of $5.3^\circ$ to the freestream. These conditions were selected as being analogous to the full-scale descending flight condition that yields maximum BVI noise radiation. The focus of the test was on three different flight cases: a baseline (BL) case with conventional control inputs and two cases with higher-harmonic control (HHC) inputs applied to the rotor at a frequency of three cycles per rotor revolution [the so-called minimum-vibration (MV) and minimum-noise (MN) cases]. Further operational parameters for the test are summarized in Table 1. A detailed description of the rotor model and the measurement procedures used in the HART II test are given in [1–4].

### B. Computational Model

Simulations of the HART II test cases were performed using the VTM. The present formulation of the VTM, developed by Brown and Line [12,13], couples a model for the aerodynamics of the blade to an Eulerian representation of the dynamics of the vorticity in the flowfield.

#### *1. Wake Model*

In the VTM, the vorticity in the flowfield is evolved by solution of the Navier–Stokes equations in vorticity–velocity form on a structured Cartesian grid surrounding the rotor. Assuming incompressible flow with velocity $\mathbf{u}$, the associated vorticity distribution $\omega = \nabla \times \mathbf{u}$ evolves according to the unsteady vorticity transport equation,

**Table 1 Rotor operational parameters**

| Parameter | Value |
|---|---|
| Forward velocity | 33 m/s |
| Rotational speed | 1041 rpm |
| Blade passage frequency | 69.4 Hz |
| Shaft tilt | $5.3^\circ$ |
| Thrust coefficient | 0.00457 |
| Advance ratio | 0.151 |

**Table 2 Computational resolution**

| | Size of smallest cells | | Time steps per rotor revolution | Degrees per time step |
|---|---|---|---|---|
| Coarse | $R/55.5$ | $c/3.36$ | 350 | 1.03 |
| Medium | $R/83.3$ | $c/5.04$ | 525 | 0.69 |
| Fine | $R/125.0$ | $c/7.56$ | 800 | 0.45 |

$$\frac{\partial}{\partial t}\omega + \mathbf{u}\cdot\nabla\omega - \omega\cdot\nabla\mathbf{u} = S + \nu\nabla^2\omega \tag{1}$$

In this formulation, the vorticity then becomes the conserved variable within the flow, and thus is not affected by the numerical dissipation that is inherent in CFD codes based on a pressure-velocity formulation of the Navier–Stokes equations. In addition, the local rate of numerical diffusion is controlled very effectively by using a set of highly compressive flux limiters within the particular implementation of Toro's weighted average flux method [14] that is used within the code to convect the solution through time. At each time step, the velocity at the cell faces is obtained from the vorticity distribution using a fast multipole technique to invert the differential form of the Biot–Savart equation,

$$\nabla^2\mathbf{u} = -\nabla\times\omega \tag{2}$$

An adaptive grid is used to track the evolving vorticity in such a way that cells only exist in regions of the computational domain where the vorticity is nonzero. As the vorticity moves to a new location, new cells are created, and any cells that no longer contain vorticity are destroyed. Thus, the grid structure is free to follow the evolution of the wake, eliminating the requirement for explicit numerical boundary conditions at the edge of the computational domain and increasing the computational efficiency of the method. Moreover, a nested grid system allows for fine resolution close to the

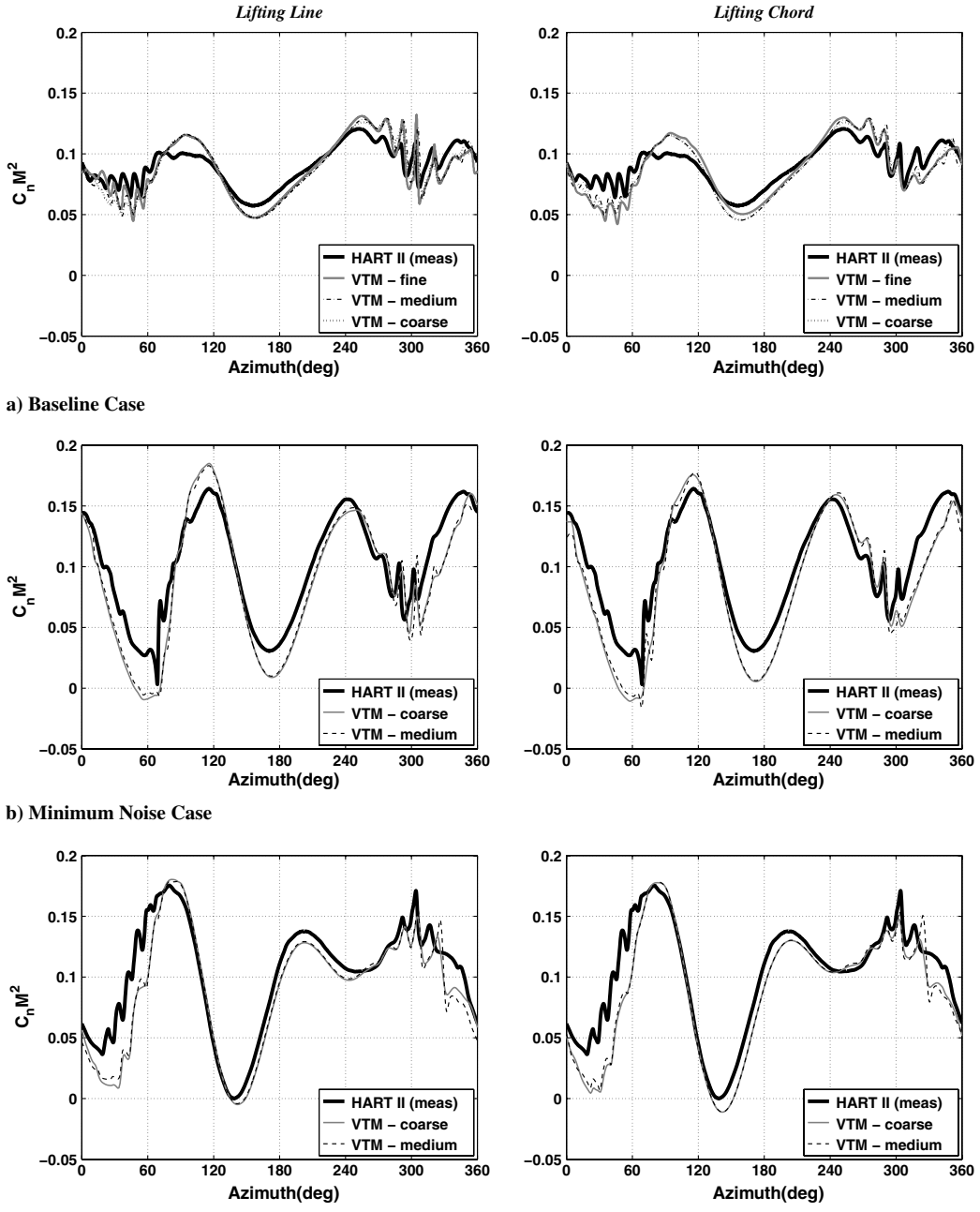


**Fig. 1 Comparison of blade loading $C_N M^2$ at 87% span, as predicted using lifting-line and lifting-chord representations of the blade aerodynamics, against experimental data for all three HART II flight cases.**

rotor and then a systematic decrease in resolution with distance from the rotor hub.

*2. Blade Aerodynamic Model*

Two separate blade models have been incorporated within this VTM framework in order to yield the aerodynamic loading on the blades. In the first model, an extension of the Weissinger-L formulation of the lifting-line theory is implemented by dividing the length of each rotor blade into a series of discrete panels. A bound vortex is attached to the quarter-chord of each panel. The strength of the bound vorticity along the length of the blade is then determined by simultaneously enforcing a condition of zero throughflow at a set of collocation points that are located at the three-quarter-chord of each panel.

A second model for the blade aerodynamics is based on an extension of the classical unsteady thin aerofoil theory and uses a particular formulation for the airloads that is based on that developed in state-space form for flexible aerofoils by Peters et al. [15]. The zero-throughflow boundary condition allows the total bound circulation on each blade panel to be written as

$$\Gamma = 2\pi b\left[f(w_0 - \lambda_0) + \tfrac{1}{2}(w_1 - \lambda_1)\right] \tag{3}$$

where $f$ is a reverse flow parameter designed to enforce the Kutta condition at the downwind edge of the aerofoil. The circulation is defined in terms of the weighted integrals, given by

$$\lambda_n = \frac{1}{K_n}\int_0^\pi \lambda \cos^n\varphi \, \mathrm{d}\varphi \tag{4}$$

and

$$w_n = \frac{1}{K_n}\int_0^\pi w \cos^n\varphi \, \mathrm{d}\varphi \tag{5}$$

where $w$ is the component, normal to the blade chord, of the blade velocity relative to the uniform background flow and $\lambda$ is the component, again normal to the blade chord, of the velocity that is induced by all vorticity in the computational domain, except that which is bound to the panel under consideration. The Glauert variable $\varphi$ is defined such that $x = b\cos\varphi$, where $0 \le \varphi \le \pi$ so that $-b \le x \le +b$, and

$$K_n = \int_0^\pi \cos^n\varphi \, \mathrm{d}\varphi \tag{6}$$

These integrals are evaluated numerically after evaluating the integrands at several discrete points along the chord of each blade panel. In all cases described in this paper, 11 such points were used in total: these were cosine-distributed along the chord to give enhanced resolution of the steep loading gradient near the upwind edge of the blade.

The sectional lift (per unit span) is then given by

$$L_0 = \rho U_\infty\left(\Gamma + \frac{b}{2}\lambda_1\right) + \pi\rho b^2(\dot{w}_0) \tag{7}$$

Using the same notation, the total bound circulation on the aerofoil given by the Weissinger-L method is

$$\Gamma = 2\pi b f[w - \lambda]|_{x=b/2} \tag{8}$$

and the sectional lift (per unit span) is simply

$$L = \rho U_\infty \Gamma + \pi\rho b^2 \dot{w}|_{x=0} \tag{9}$$

In all cases, 40 panels in a cosine distribution were used to resolve the spanwise variation in loading along the length of the blade. In both aerodynamic models, the trailed and shed vorticities from each vortex panel are added to the near wake downstream of the blade as the local vorticity source

$$S = -\boldsymbol{\tau}\frac{\partial\Gamma}{\partial t} + \mathbf{u}_b\frac{\partial\Gamma}{\partial r} \tag{10}$$

where $\boldsymbol{\tau}$ is the unit vector parallel to the downwind edge of the blade and $\mathbf{u}_b$ is the velocity of the downwind edge relative to the air. Most important in the present context, the shed vorticity distribution behind the blade is fully resolved using this approach. Its influence on the unsteady aerodynamic response of the system is thus captured directly in the simulations without the need to resort to empirical modeling of the indicial response of the blade, as is done in some comprehensive codes in order to compensate for their under-resolution, oversimplification of the geometry, or even omission in

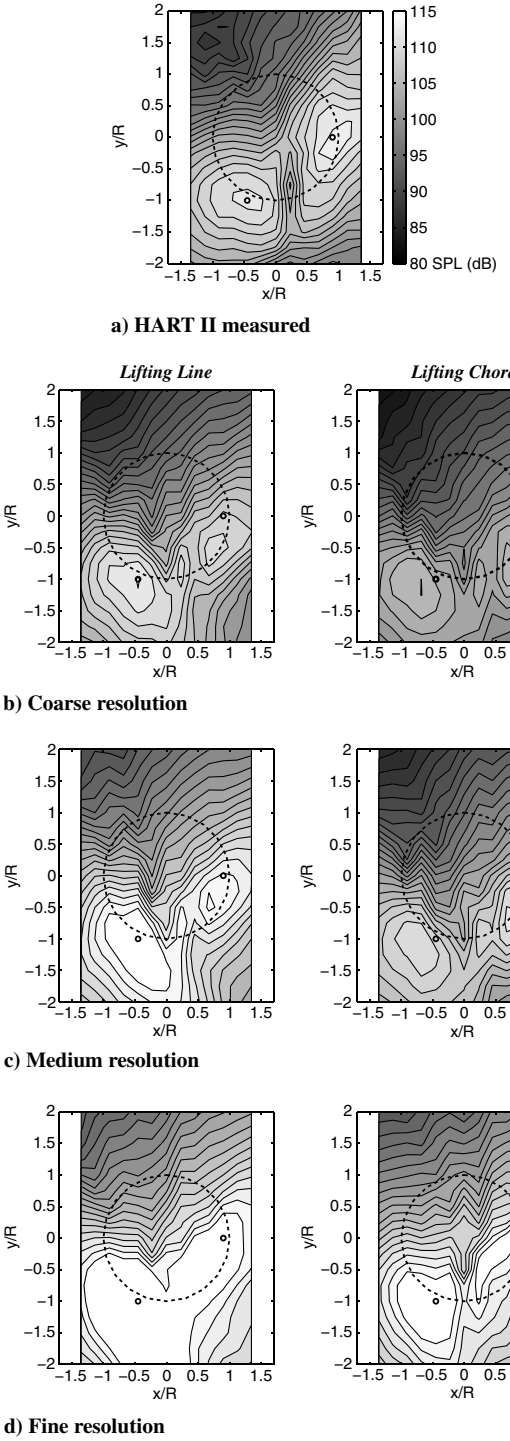


**Fig. 2 Predicted and measured SPL noise contours for the HART BL flight case. (The rotor position is marked by a dashed circle.)**

some cases of the sheet of vorticity that is shed into the flow immediately behind the blades.

The two-dimensional aerodynamic characteristics of the rotor blade sections are specified in a lookup table as a function of angle of attack and Mach number for a given Reynolds number. These characteristics can be used to precondition the zero-throughflow boundary condition to allow the blade aerodynamic calculation to closely match the sectional aerodynamic characteristics, including stall, of the actual blade. As this approach is still essentially inviscid, the profile drag of the blade is calculated as a separate function of local angle of attack and is then added to the local aerodynamic force that is calculated from the blade aerodynamic model.

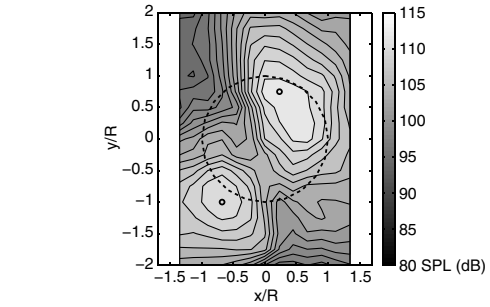


**a) HART II measured**

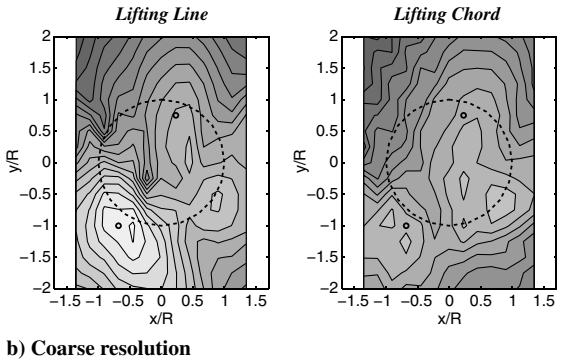


**b) Coarse resolution**

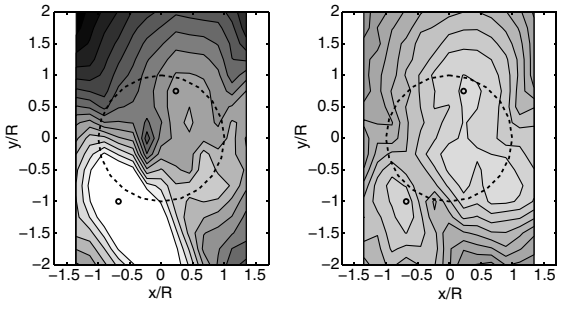


**c) Medium resolution**

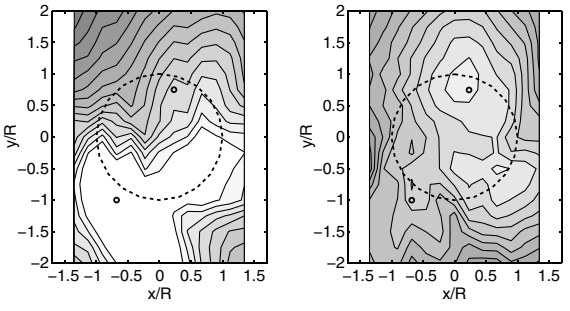


**d) Fine resolution**

**Fig. 3 Predicted and measured SPL noise contours for the HART MN flight case. (The rotor position is marked by a dashed circle.)**

*3. Fuselage Model*

Fuselages or other solid bodies are represented using an unsteady vortex panel method, as described in [16]. The surface of any body immersed in the flowfield is discretized into a system of panels, such that each panel edge is represented as a vortex filament with constant strength, forming a closed loop of vorticity. The velocity at the centroid of any panel is calculated as the sum of the influences from all vortex filaments on the body together with the velocity induced by all the other vorticities within the flow. To determine the strengths of the vortex loops, a boundary condition of zero throughflow is enforced simultaneously at the centroids of all panels. Where present in the simulations described in this paper, the drive housing for the HART II rotor was modeled using 1908 panels. This yields a level of resolution that is comparable to previous simulations using this approach: for example, as described in [16].

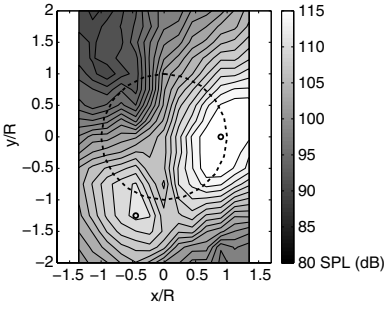


**a) HART II measured**

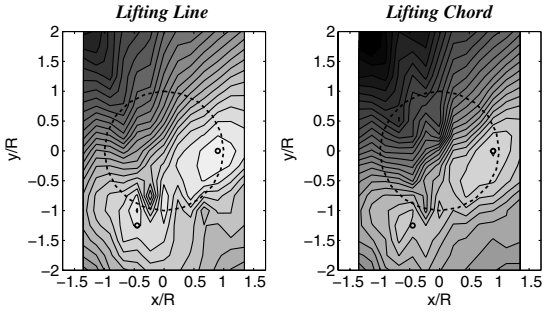


**b) Coarse resolution**

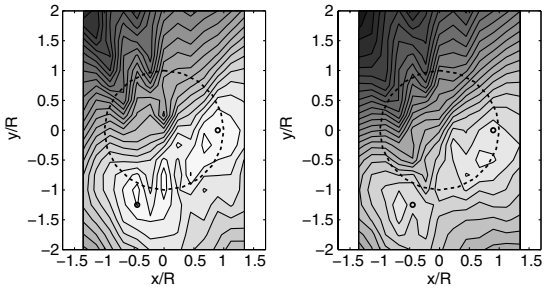


**c) Medium resolution**

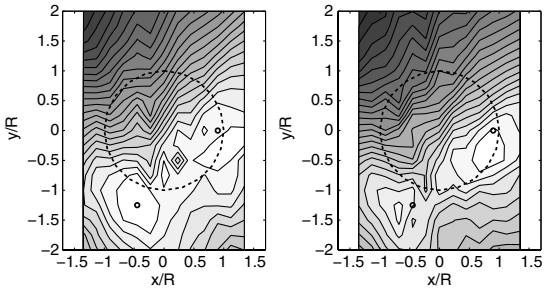


**d) Fine resolution**

**Fig. 4 Predicted and measured SPL noise contours for the HART MV flight case. (The rotor position is marked by a dashed circle.)**

*4. Structural Dynamics*

In the particular version of the model that was used in the present investigation, the motion of the blades is prescribed based on a variable-separable interpolation of the blade deformations that were measured at discrete azimuthal and radial locations on each blade during the HART II experiment. In the experiment, the blade deformation was measured using a nonintrusive optical method called stereo pattern recognition, as described in [17–19].

Each component $D$ of the blade deformation is reconstructed in the simulations by using interpolating functions of the form

$$D(r,\psi) = \sum_{i=1}^{N_r}\sum_{j=1}^{N_a} a_{ij} P_i(r) F_j(\psi) \tag{11}$$

where $N_r$ and $N_a$ are, respectively, the number of radial and azimuthal interpolation functions $P_i(r)$ and $F_j(\psi)$, used to describe the particular components of the blade deflection. The radial interpolation functions were taken to be polynomials, and the azimuthal interpolation functions were taken to be the components of a Fourier series so that

$$P_i(r) = r^{(i-1)} \tag{12}$$

and

$$F_j(\psi) = \begin{cases} \cos\dfrac{j-1}{2}\psi, & \text{if } j \in \{1,3,5,\cdots\} \\ \sin\dfrac{j}{2}\psi, & \text{if } j \in \{2,4,6,\cdots\} \end{cases} \tag{13}$$

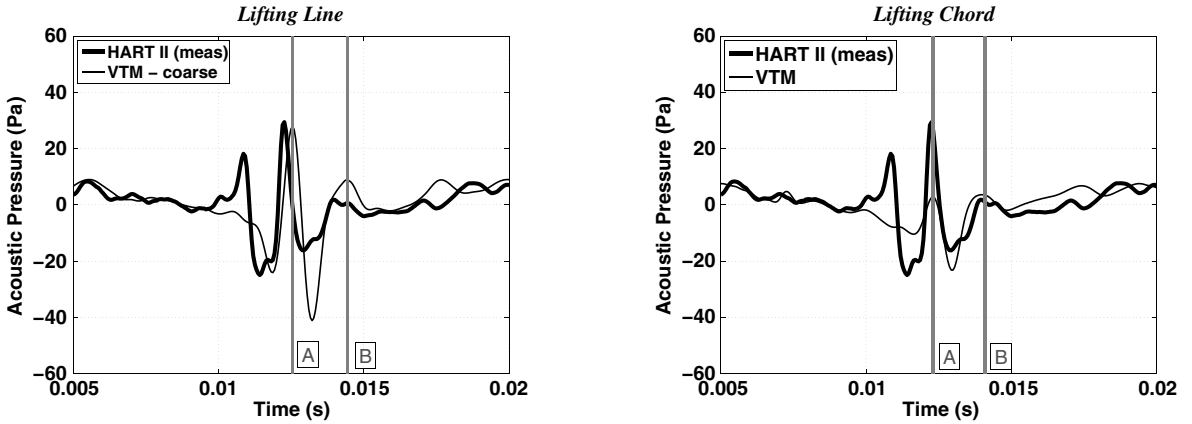


**a) Time history of acoustic pressure for a single blade passage**

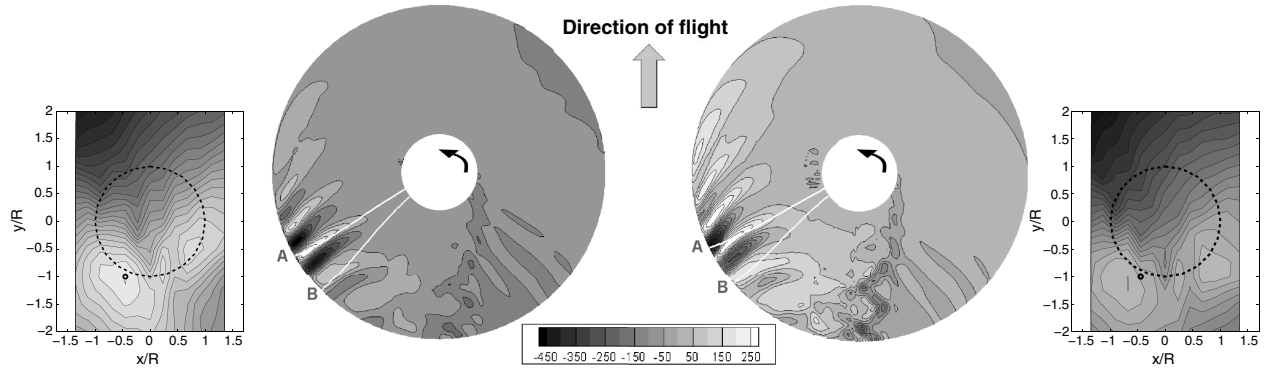


**b) Predicted acoustic source density (loading noise, Pa/m$^3$)**

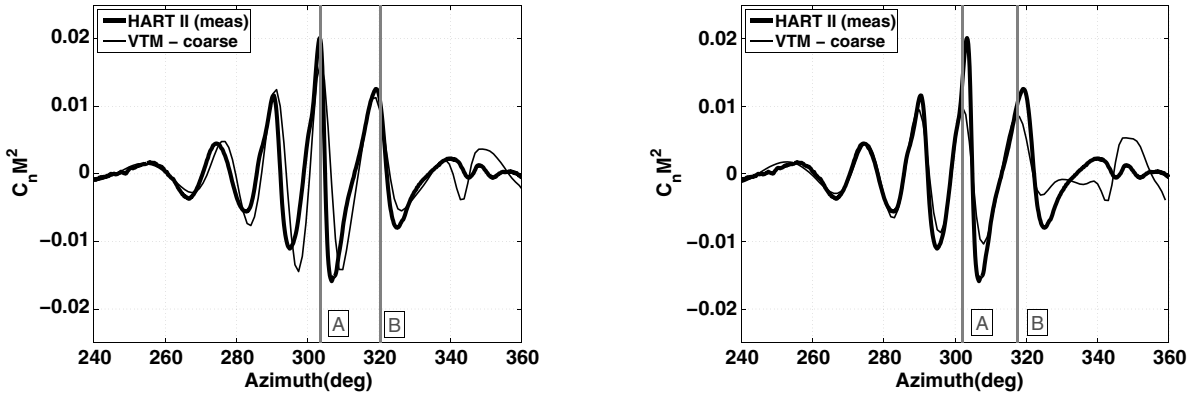


**c) BVI-induced airloads**

**Fig. 5 Time history of acoustic pressure for one blade passage and the corresponding BVI-induced airloads and source density distribution on the rotor for an observer (marked by small circle) located at the experimentally measured SPL maximum on the retreating side of the rotor (HART II BL case). Numerical results are for the coarse computational resolution.**

The coefficients $a_{ij}$ of the interpolation function were calculated by enforcing a simple least-squares fit to the measured data for the blade deformations. This method interpolates over the relatively sparse experimental data, as well as fills any gaps in the data where the markers used in the measurements could not be viewed because they lay within the shadow of the drive enclosure and the mounting support or had peeled off the blades. Throughout, the structural dynamics of the blades were prescribed using six interpolation functions in the radial direction and nine in the azimuthal direction. The sets of coefficients that give the best approximation to the elastic flap, lag, and torsional deformations, $z_{el}$, $y_{el}$, and $\theta_{el}$, of each of the blades when using a basis with these dimensions are given in [9] for the HART II BL test case.

The difference between the interpolation and the experimental data set for each of the measured components of the elastic deformation of the blades was within the stated error bounds on the measurements of $\pm 0.5°$ for the elastic torsion and $\pm 0.5$ mm for the flap and lag deflections. Nevertheless, the reliability of the interpolation may be questioned in areas where the experimental data were particularly sparse, as was, for instance, the case around 0 and 180° azimuth.

### C. Acoustic Analysis

The acoustic field that is radiated by the rotor is computed using a postprocessor for the blade aerodynamic loads that implements the Farassat-1A formulation [20] of the Ffowcs Williams–Hawkings

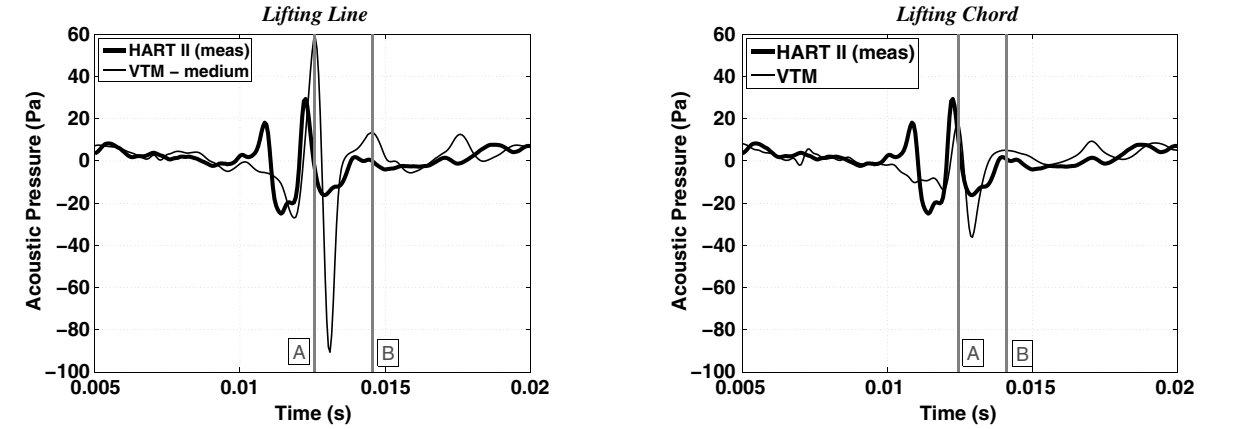


a) Time history of acoustic pressure for a single blade passage

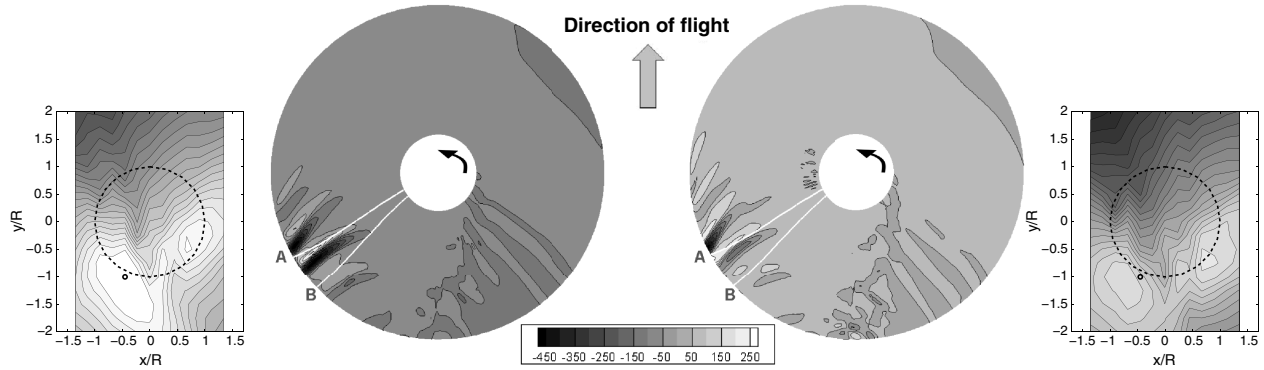


b) Predicted acoustic source density (loading noise, Pa/m$^3$)

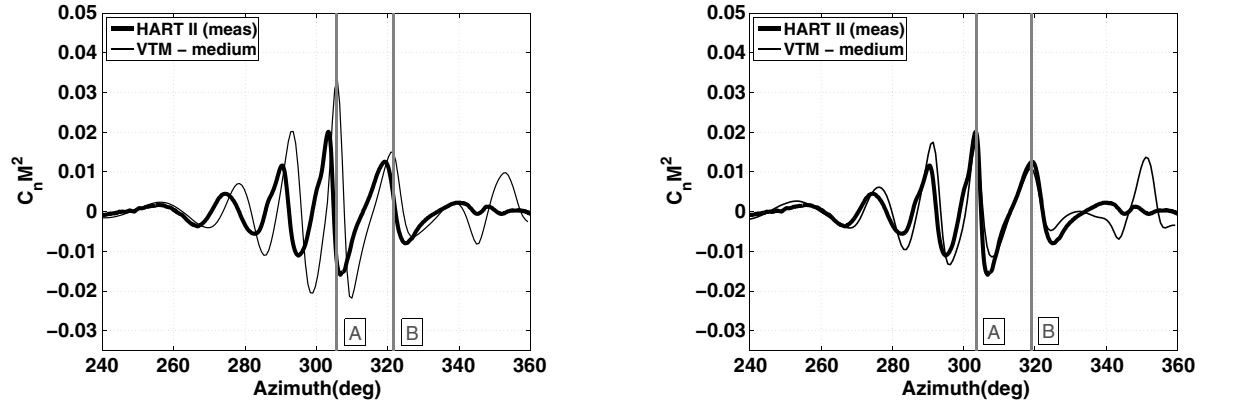


c) BVI-induced airloads

**Fig. 6 Time history of acoustic pressure for one blade passage and the corresponding BVI-induced airloads and source density distribution on the rotor for an observer (marked by small circle) located at the experimentally measured SPL maximum on the retreating side of the rotor (HART II BL case). Numerical results are for the medium computational resolution.**

(FW–H) equation [21]. This formulation is widely used in rotor acoustic calculations because of the efficiency and accuracy that results from its analytic representation of the observer time derivatives. The acoustic pressure $p'$ at a point $\mathbf{x}$ at time $t$ can be written as

$$p'(\mathbf{x},t) = \frac{1}{4\pi}\frac{\partial}{\partial t}\iint_S \left[\frac{\rho v_n}{r(1-M_r)}\right]_\tau \mathrm{d}S + \frac{1}{4\pi a_0}\frac{\partial}{\partial t}\iint_S \left[\frac{F_r}{r(1-M_r)}\right]_\tau \mathrm{d}S + \frac{1}{4\pi}\frac{\partial}{\partial t}\iint_S \left[\frac{F_r}{r^2(1-M_r)}\right]_\tau \mathrm{d}S \quad (14)$$

where $a_0$ is the speed of sound and $\mathbf{r}$ is the distance between the point $x$ and the acoustic source. $F_r$ is the component of local force that is exerted by the body on the fluid, and which acts in the direction of the observer ($F_r = \mathbf{F}\cdot\mathbf{r}$). $M_r$ is the Mach number at which the source is moving relative to the observer ($M_r = \mathbf{M}\cdot\mathbf{r}$). The source time $\tau$, also known as the retarded time, is the time at which the sound wave is emitted from the source relative to the observer time $t$. This accounts for the finite length of time that is required for the acoustic waves to reach the observer point from the location where they have been emitted.

The total noise includes contributions from loading, thickness, and quadrupole sources. Thickness noise is caused when a moving rotor blade of finite thickness displaces fluid particles and, as a result, produces a pressure change and an associated noise contribution. This is represented by the first term in Eq. (14), where $v_n$ is the local normal velocity of the blade surface. The second and third terms correspond to the far-field and near-field contributions by the loading

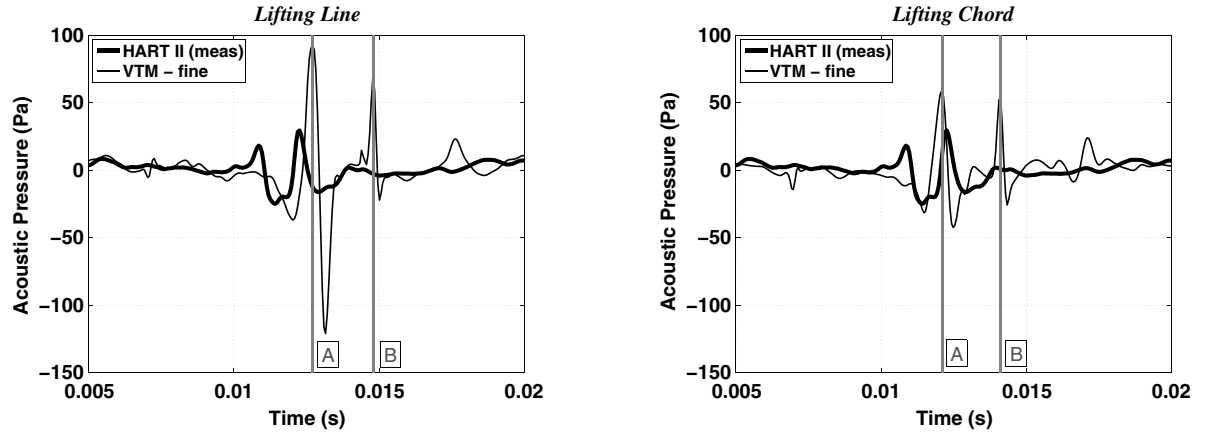


a) Time history of acoustic pressure for a single blade passage

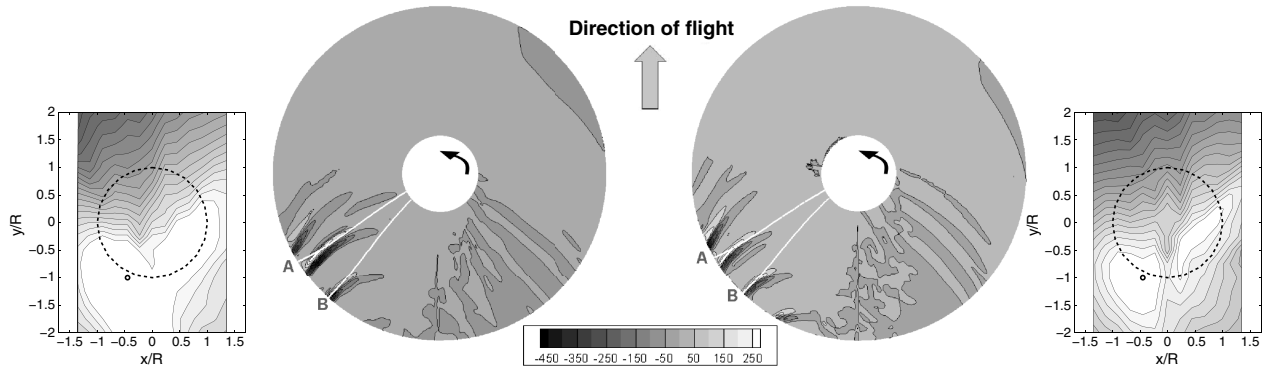


b) Predicted acoustic source density (loading noise, Pa/m$^3$)

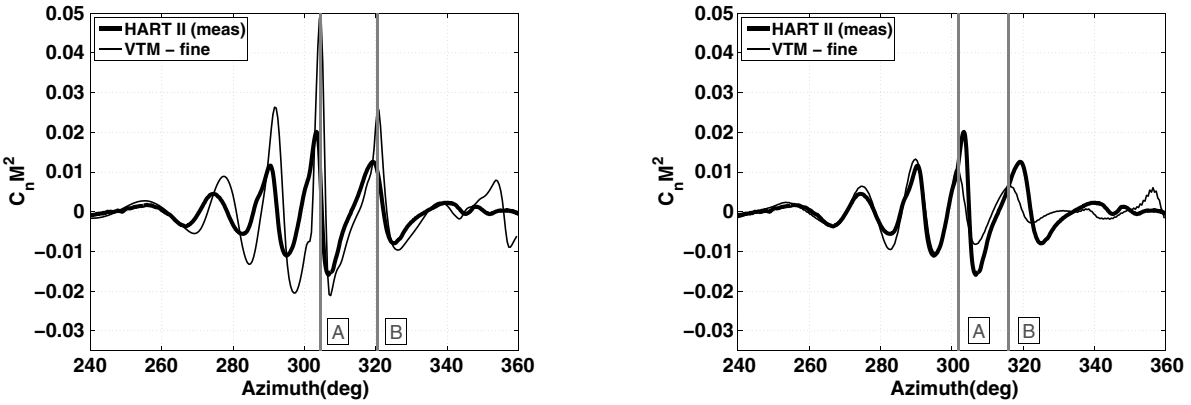


c) BVI-induced airloads

**Fig. 7 Time history of acoustic pressure for one blade passage and the corresponding BVI-induced airloads and source density distribution on the rotor for an observer (marked by small circle) located at the experimentally measured SPL maximum on the retreating side of the rotor (HART II BL case). Numerical results are for the fine computational resolution.**

noise. The loading noise is caused by the force exerted on the fluid by the moving blade surface. The contribution by the loading noise to the far-field acoustic signature of the rotor is dependent on the rate of change of the pressure on the blade and, if a compact source is assumed, can be directly related to the time rate of change of the force on the blade. It is thus clear that the highly impulsive change in lift generated by the blade encountering a vortex will have a significant impact on the acoustic signature of the rotor.

Considerable simplification is indeed introduced into the analysis by assuming that the distribution of sources of sound on the blade is acoustically compact in the chordwise direction. An acoustic source is said to be compact if its size is small relative to the wavelength of the sound waves that it generates. This assumption is justified in the present work because of the high aspect ratio of the blades and the fact that only the far-field acoustic signature is considered: in which case, the phase difference between sounds that are radiated from sources at different locations along the chord of the blade can be assumed to be minimal. The chordwise distribution of noise sources that are due to loading can then be approximated as a point source.

The blade surface in the aerodynamic model is represented by a series of panels. The aerodynamic force contributed by each blade panel is used to construct a point acoustic source at the center of each panel. The loading noise at any given observer location is then obtained by summation of these acoustic sources. The aerodynamic model assumes an infinitesimally thin blade; the thickness noise thus has to be modeled independently. This is done by attaching a source-sink pair to each blade panel. The quadrupole source term accounts for nonlinear effects (e.g., nonlinear wave propagation and steepening, variations in the local sound speed induced by compressibility, and noise generated by shocks, vorticity, and

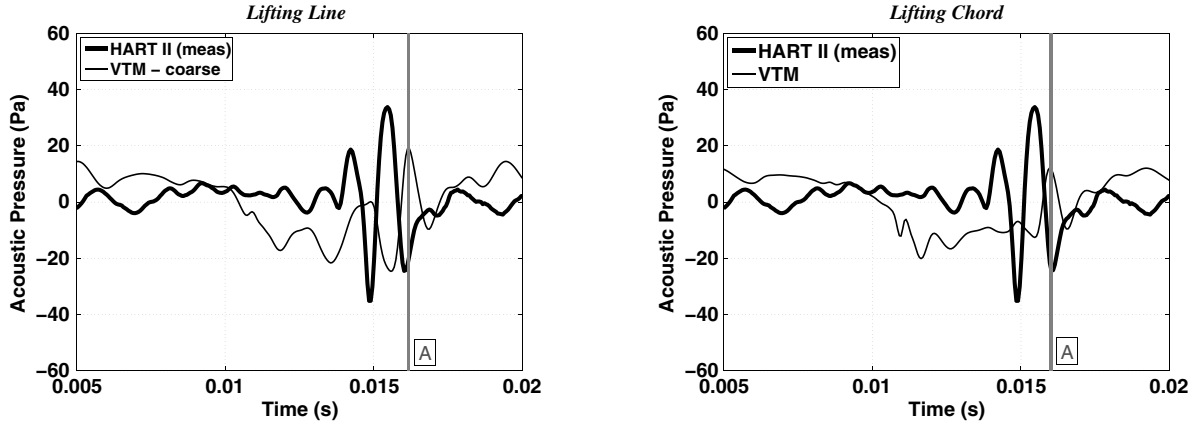


a) Time history of acoustic pressure for a single blade passage

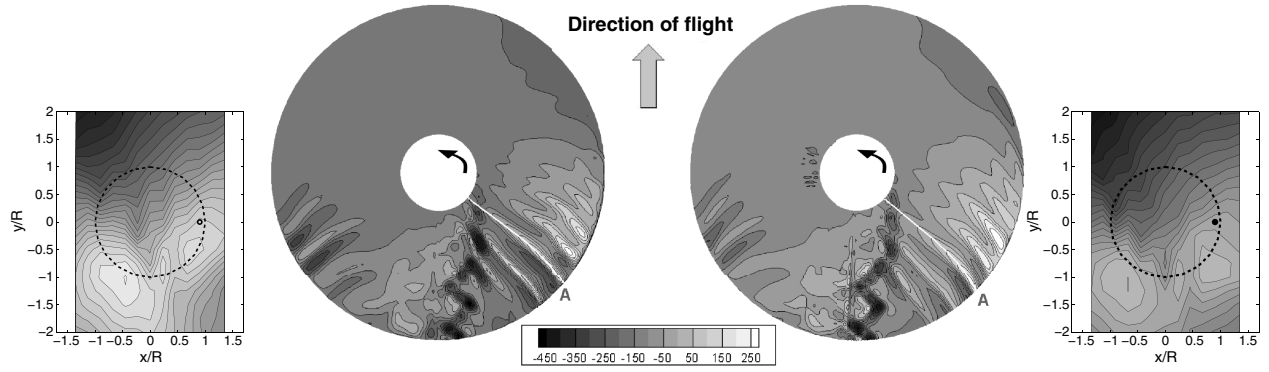


b) Predicted acoustic source density (loading noise, Pa/m$^3$)

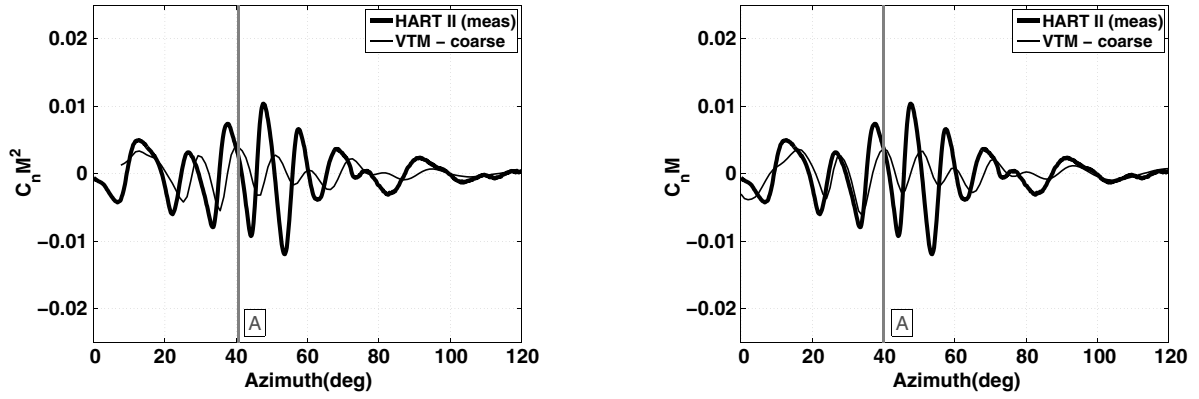


c) BVI-induced airloads

**Fig. 8 Time history of acoustic pressure for one blade passage and the corresponding BVI- induced airloads and source density distribution on the rotor for an observer (marked by small circle) located at the experimentally measured SPL maximum on the advancing side of the rotor (HART II BL case). Numerical results are for the coarse computational resolution.**

turbulence in the flowfield). Although this term is known to play an important role in BVI noise generation, particularly at higher tip Mach numbers, it is not easily computed in any computational approach that uses a blade-surface-based methodology to compute the aerodynamics of the rotor. Indeed, historically, the usual recourse in such methods has been to omit the quadrupole term entirely from the acoustic model, and our formulation has followed suit. Given that the tip Mach number of the HART II rotor was approximately 0.76 and, thus, that compressibility effects must have been important over at least parts of the blade, it is important to acknowledge the omission of this term from our analysis as a possibly significant source of systematic error in the predictions that are presented later in this article. No account has been made for absorption and scattering due to the presence of bodies that are immersed in the flowfield, such as the experimental drive enclosure in the HART II test, even when it was included in the aerodynamic calculation.

## III. Airload Predictions

The results of VTM calculations are compared for the three flight cases of the HART II test: the BL case with conventional control inputs and the two cases with HHC inputs applied to the rotor (the so-called MV and MN cases). In all cases, the rotor was trimmed to the experimental thrust coefficient and to zero aerodynamic pitch and roll moments about its hub.

A detailed description of the influence of grid resolution and time step on the ability of the lifting-line and lifting-chord models to resolve the unsteady aerodynamics of the rotor blade is given in [22].

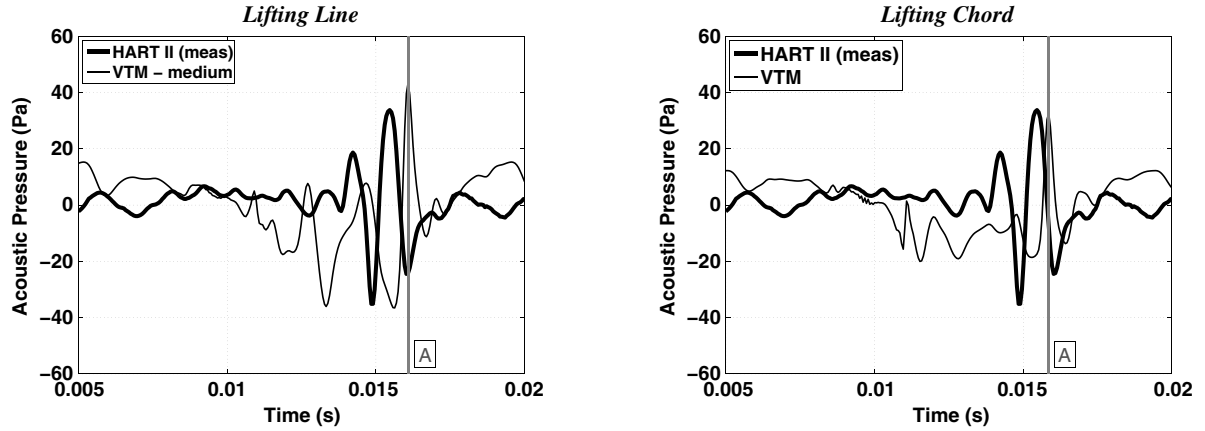


a) Time history of acoustic pressure for a single blade passage

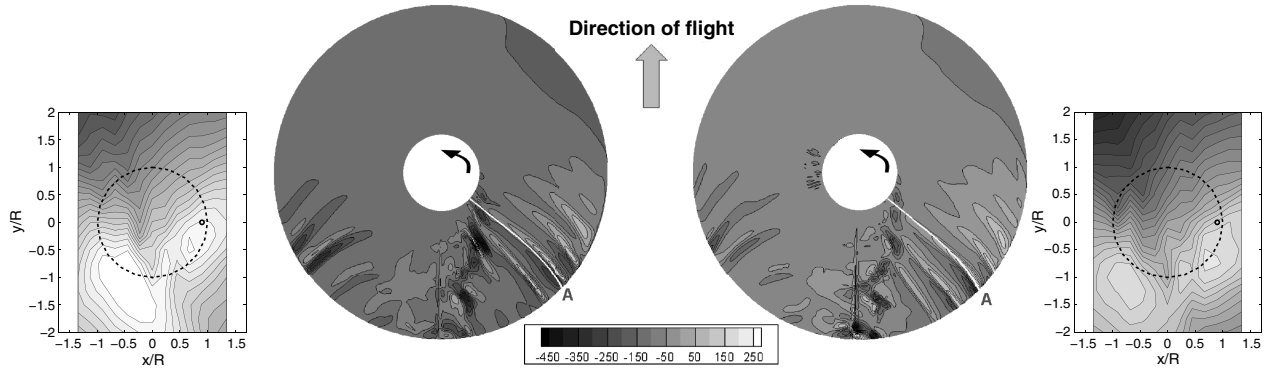


b) Predicted acoustic source density (loading noise, Pa/m$^3$)

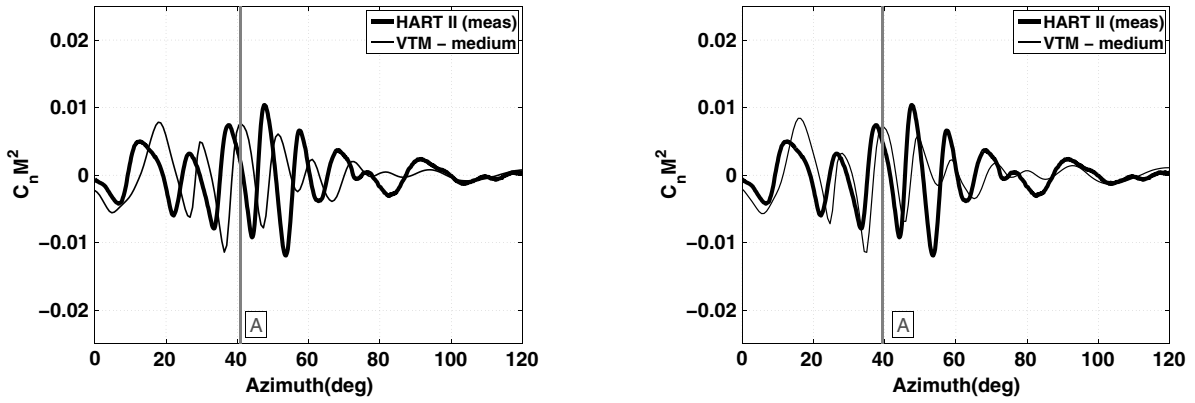


c) BVI-induced airloads

**Fig. 9 Time history of acoustic pressure for one blade passage and the corresponding BVI-induced airloads and source density distribution on the rotor for an observer (marked by small circle) located at the experimentally measured SPL maximum on the advancing side of the rotor (HART II BL case). Numerical results are for the medium computational resolution.**

In the present computations, the time step was set so that the tip of the blade would advance no further than the edge length of a single cell during a single time step. The cell edge length in the simulations was then set to always be smaller than the blade chord; together, these two conditions ensure that the distribution of vorticity within the computational domain is always adequately resolved by the numerical procedure that is used to calculate the boundary conditions for the blade aerodynamic model.

In all computations presented here, the viscosity $\nu$ in Eq. (1) was set to zero, and thus the VTM was run in essentially inviscid mode. Under these conditions, the size of the computational cells, rather than any physical process, sets the fundamental lower limit on the size of the smallest vortical structures that can be resolved within the computational domain. Simulations of the HART II BL case at three different spatial and temporal resolutions (as summarized in Table 2) and simulations of the MN and MV cases at two of the three different resolutions were compared to expose the effect of grid resolution in such an approach on the ability of each of the blade models described earlier to predict the acoustic signature of the HART II rotor.

During the HART II test program, the sectional airload $C_N$ at 87% of the blade span was estimated by conditionally averaging the signal from a set of pressure transducers mounted at this section of the blade. Figure 1 compares the measured blade airload at this radial station for the three HART II flight cases, expressed in terms of normal force coefficient $C_N M^2$, to the loading predicted by the VTM. In general, the calculated loading on the rotor compares reasonably well with the experimental data for all flight cases.

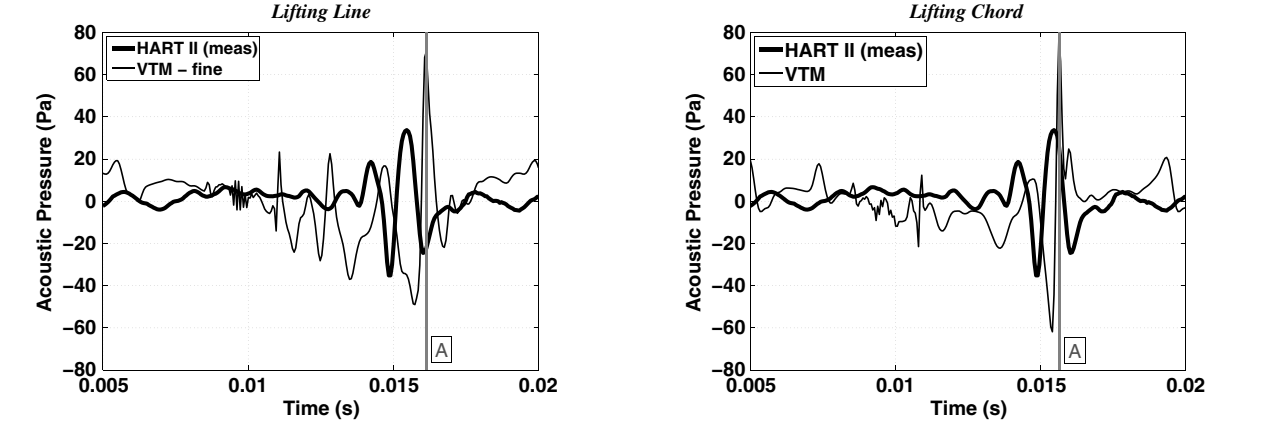


**a) Time history of acoustic pressure for a single blade passage**

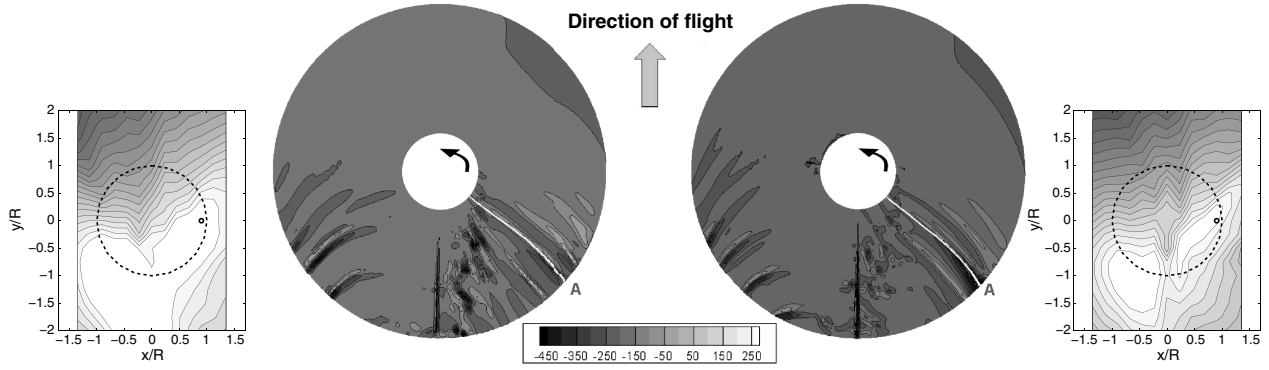


**b) Predicted acoustic source density (loading noise, Pa/m$^3$)**

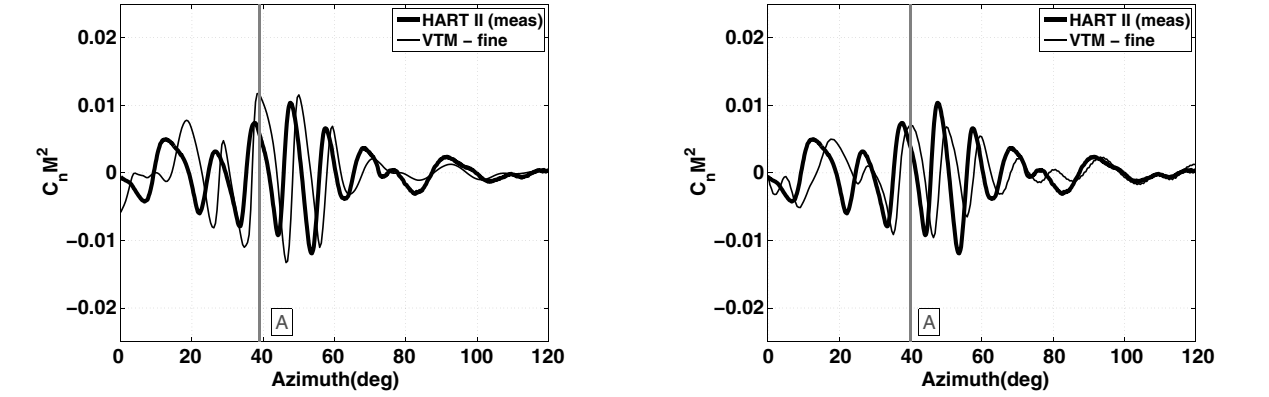


**c) BVI-induced airloads**

**Fig. 10 Time history of acoustic pressure for one blade passage and the corresponding BVI-induced airloads and source density distribution on the rotor for an observer (marked by small circle) located at the experimentally measured SPL maximum on the advancing side of the rotor (HART II BL case). Numerical results are for the fine computational resolution.**

The advancing side is perhaps the least well resolved, with the largest discrepancies between prediction and experiment on this side of the disk occurring in the low-frequency component of the airload. The discrepancies in this component of the airload are similar, regardless of computational resolution and irrespective of the model that is used to represent the aerodynamics of the blade. As it is this component of the loading that is primarily affected by control inputs and blade structural deformation, it is most likely that these discrepancies are due to errors in the interpolation that was used to prescribe the blade dynamics within the simulation, as discussed in [9–11].

The predictions of the loading on the retreating side of the disk correlate well with the experimental data for all three flight cases. The figures nevertheless show that the lifting-line method is more sensitive to changes in the cell size used to represent the wake than the lifting-chord approach. Indeed, as described in more detail in [9–11], the differences between the predictions of the two models are most obvious in their representation of the high-frequency components of the blade airload.

## IV. Acoustic Predictions

### A. Sound Pressure Levels

The accuracy of the airload predictions, particularly of the loads that are induced by BVIs, directly influences the accuracy to which the acoustic signature of the rotor can be predicted. In the HART II experiment, noise measurements were performed with an array of 13 microphones mounted transversally to the axis of the tunnel on a measurement plane that was located 2.215 m (1.1$R$) below the rotor hub. A map of the sound intensity on the measurement plane was generated by moving this microphone array along the axis of the tunnel. These data can be used effectively to determine the influence of the airload predictions on the position and amplitude of the predicted sound pressure maxima on both the advancing and retreating sides of the rotor disk. The positions of each of the acoustic maxima and any regions of decay determine the overall directivity of the noise produced by the rotor. The directivity of the noise can be assessed qualitatively by comparing the predicted distribution of sound intensity below the rotor to that measured during the HART II experiment.

Figures 2–4 compare the measured sound pressure level (SPL) on the measurement plane located at 1.1$R$ below the rotor hub to that computed from the airloads that were predicted by the VTM. The acoustic field that is radiated by the rotor is computed using a postprocessor for the blade aerodynamic loads that implements the Farassat-1A formulation [20] of the FW–H equation [21], as described in Sec. II.C. In all cases, the data have been filtered to include only the range of frequencies between 6–40 times the blade passage frequency. This is generally accepted to be the range that is dominated by BVI noise.

The acoustic calculation does not account for the scattering and absorption of acoustic energy by solid bodies within the flow and, while this does not affect the principal sources of sound in the flowfield, it does influence the distribution of noise once it reaches the measurement plane. This deficiency is visible in Fig. 2 for the BL case, for example, where scattering and absorption by the drive enclosure (fuselage) is most likely responsible for the thin region of reduced noise that is present in the experimental data (Fig. 2a) in the center and to the rear of the rotor disk, but which is not captured by the numerical method (Fig. 2b–2d).

For all three of the HART II flight cases, the distribution of acoustic pressure on the measurement plane is characterized by two acoustic maxima that occur: one on the advancing side and one on the retreating side of the disk. The sound pressure can also be seen to decay rapidly upstream of the rotor toward the retreating side of the disk. The experimental results show the maximum SPL on the measurement plane to be lower in the MN case than in the BL case and the directivity to be shifted toward the front of the rotor. In contrast, the maximum SPL in the MV case is higher, but the directivity pattern is similar to that of the BL case.

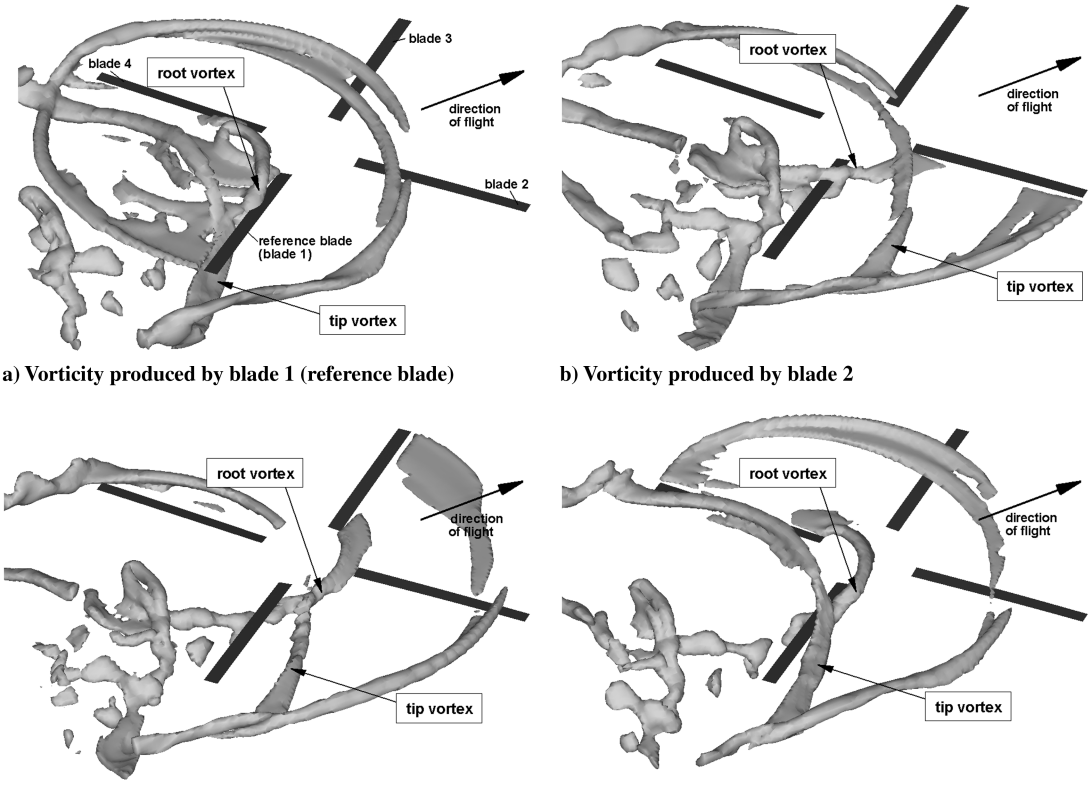


a) Vorticity produced by blade 1 (reference blade)

b) Vorticity produced by blade 2

c) Vorticity produced by blade 3

d) Vorticity produced by blade 4

**Fig. 11 Geometry of root and tip vortices as generated by each blade, when the reference blade lies at an azimuth of 40°, predicted by the VTM for the HART II BL case (lifting-chord model, medium computational resolution).**

In general, as is the case with the airload predictions, the SPL predicted by the VTM shows a better correlation with the measured data on the retreating side of the disk than on the advancing side. The upstream decay in the noise level on the retreating side of the rotor disk, which is present in both the BL and MV cases, is well resolved, irrespective of the aerodynamic model or the computational resolution that is used. The directivity of the sound is therefore captured well by the numerical method. The change in directivity found in the MN case compared with the BL case is also captured reasonably well by the numerics. The two SPL maxima, present in all the test cases, are also captured in the numerical predictions, albeit with some errors in their positions and peak SPL values. The SPL maximum on the retreating side of the disk is generally more accurately captured, both in terms of its position and its amplitude, than the maximum that is present on the advancing side of the disk.

Where the lifting-line approach is used to model the aerodynamics of the blades, the overprediction in the amplitude of the BVI loading, as the grid resolution is increased, translates into an overprediction of the acoustic pressure levels on the measurement plane beneath the rotor. Indeed, the peak value of the SPL at the maxima on both sides of the rotor increases significantly as the computational resolution is increased. The lifting-chord approach shows much less sensitivity to the computational resolution of the wake, with the result that the predicted peak value of the SPL, particularly at the maximum on the retreating side of the disk, compares well with the measured value. The method still does, however, overpredict the maximum noise

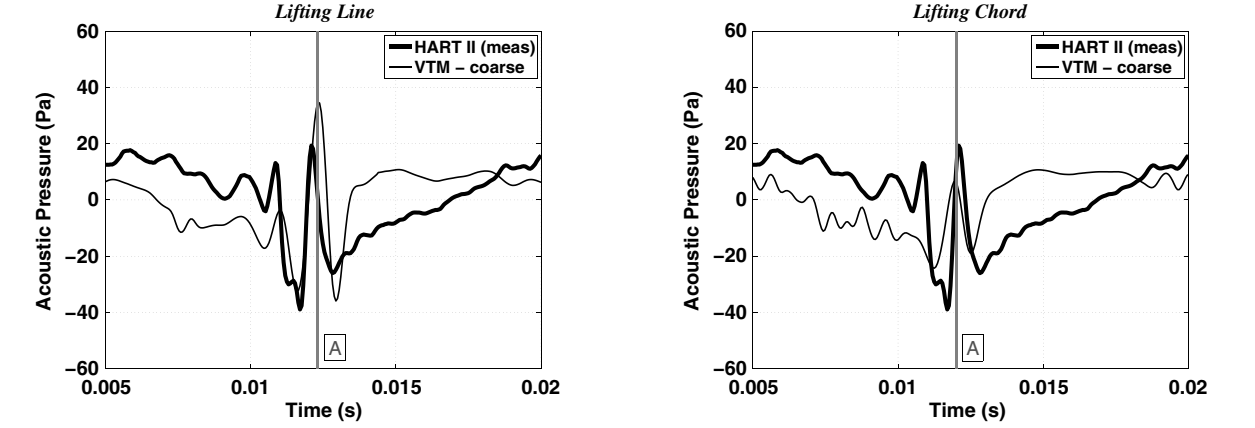


a) Time history of acoustic pressure for a single blade passage

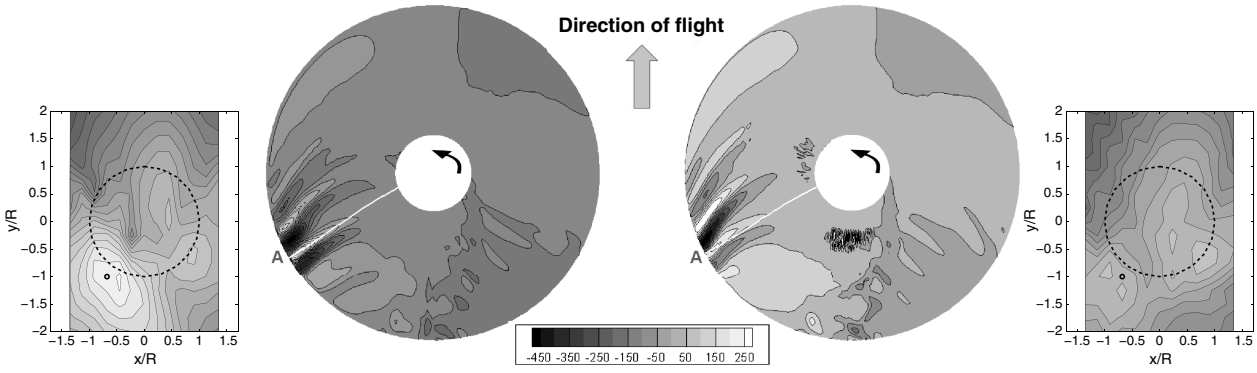


b) Predicted acoustic source density (loading noise, Pa/m$^3$)

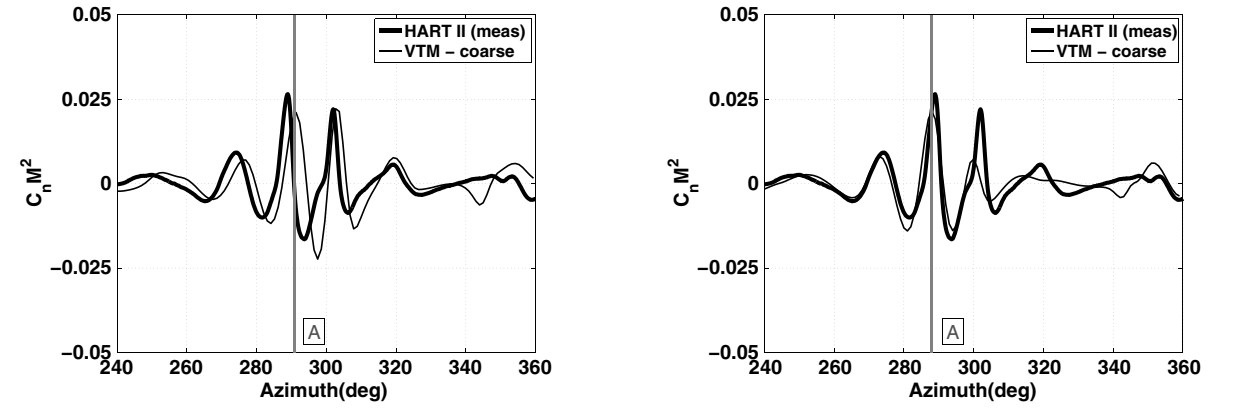


c) BVI-induced airloads

**Fig. 12 Time history of acoustic pressure for one blade passage and the corresponding BVI-induced airloads and source density distribution on the rotor for an observer (marked by small circle) located at the experimentally measured SPL maximum on the retreating side of the rotor (HART II MN case). Numerical results are for the coarse computational resolution.**

levels when the finest computational resolution is used, although to a much lesser extent than when the lifting-line approach is adopted.

The reason for this behavior is relatively straightforward. As the resolution of the computation is increased, the convection algorithm used within the VTM acts to resolve the vortex core over a smaller and smaller area, with the result that the vortical structures become more and more concentrated. A smaller vortex core radius for a given vortex strength implies higher peak velocities in the vortex. These produce more impulsive changes in the loading, and thus higher noise intensity when the vortex passes close to the blade. The VTM is known to very accurately preserve the circulation in the flowfield [10] but, as this circulation is confined to fewer cells, it results in an overly impulsive acoustic pressure when the vortex interacts with the blade. While the blade airload is less sensitive to maxima and minima in the velocity profile when using the lifting-chord approach, the behavior of the acoustic postprocessing method, depending as it does on the loading gradients rather than directly on the amplitude of the BVI-loading peaks, appears to not be so benign.

The calculations at both coarse and medium resolutions predict the location of the SPL maximum on the advancing side of the rotor for all three HART II flight cases, except perhaps the MV case, to be further to the rear of the rotor disk than the position of the experimentally measured maximum. This discrepancy is marginally more apparent when the lifting-chord model is used than when the lifting-line model is used, even though the airloads are generally better predicted using the lifting-chord approach.

Several explanations for this anomaly are possible. The shift in the predicted phase of the higher-harmonic components of the blade

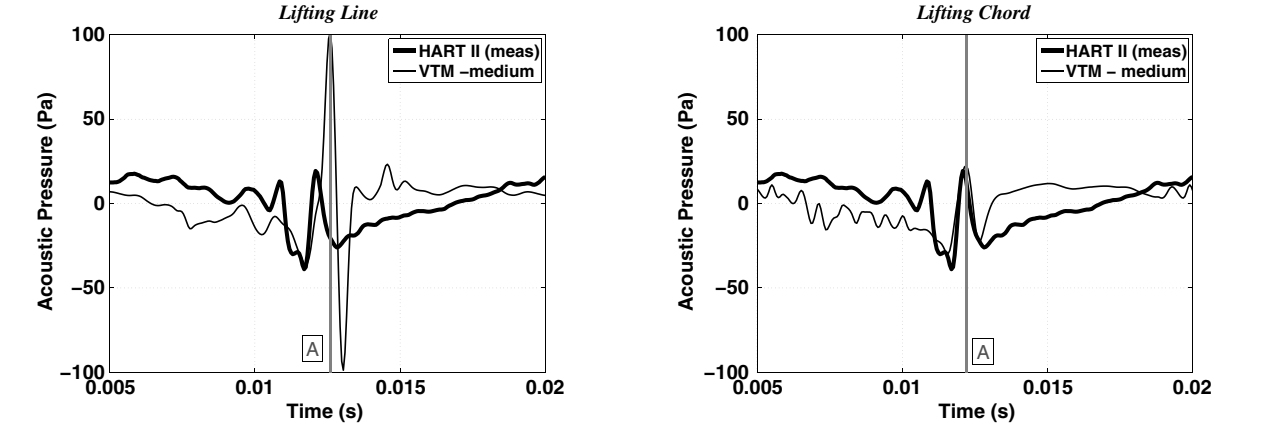


a) Time history of acoustic pressure for a single blade passage

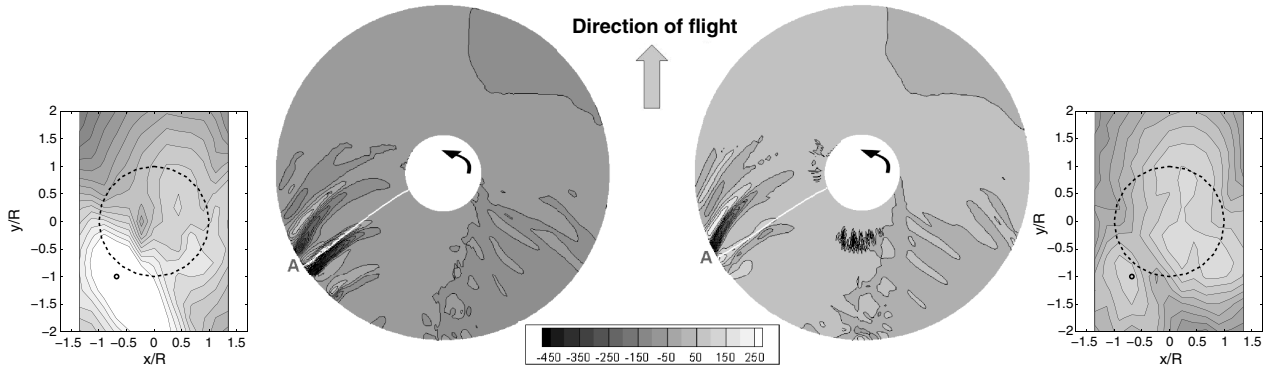


b) Predicted acoustic source density (loading noise, Pa/m$^3$)

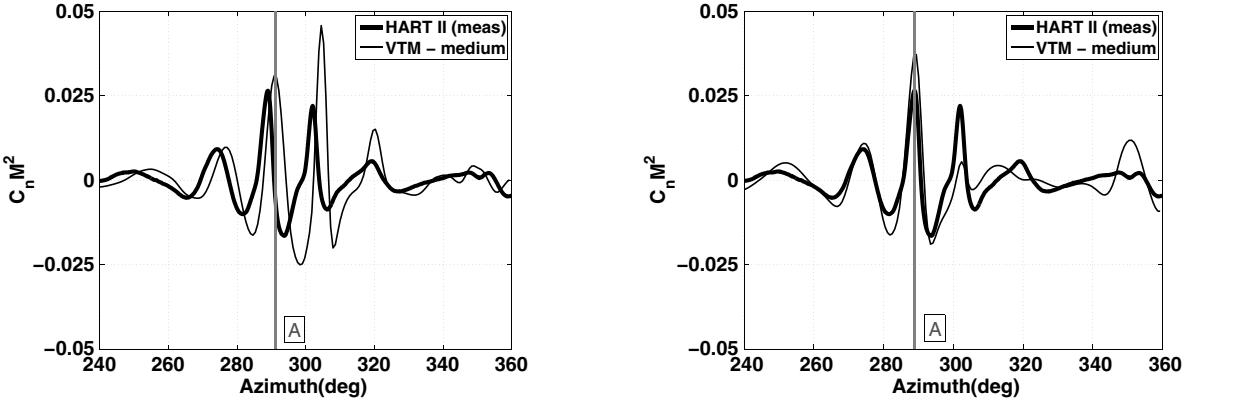


c) BVI-induced airloads

**Fig. 13 Time history of acoustic pressure for one blade passage and the corresponding BVI-induced airloads and source density distribution on the rotor for an observer (marked by small circle) located at the experimentally measured SPL maximum on the retreating side of the rotor (HART II MN case). Numerical results are for the medium computational resolution.**

airload (see later) relative to the experimental data for the advancing side of the rotor will have some effect on the location at which the maximum SPL on the measurement plane will occur. This error in phase is present when either the lifting-line or lifting-chord models are used; this explanation thus does not explain the difference that is exhibited between the acoustic predictions that are obtained using the two blade aerodynamic models.

### B. Acoustic Sources

The relationship between the noise produced at the acoustic maxima and the source of the noise in the individual BVI events on the rotor is examined in this section. Figures 5a, 6a, 7a, 8a, 9a, and 10a compare the predicted and measured time histories of acoustic pressure at the positions of the two microphones located at the points of measured maximum noise level on the advancing and retreating sides of the rotor for the BL case (microphones M11 and M4, respectively). The positions of these microphones are represented by the small circles on the acoustic SPL plot in Figs. 5b, 6b, 7b, 8b, 9b, and 10b. The time histories are produced with expanded timescale corresponding to a single blade passage. The predicted distribution of acoustic source density due to loading on the disk is also plotted (in Figs. 5b, 6b, 7b, 8b, 9b, and 10b) from the perspective of an observer located at the relevant microphone. The source density is evaluated from the loading noise term in the FW–H equations and is plotted in source time: in other words, the sources are located at their position on the disk when the sound at the particular observer time was generated. In Figs. 5b, 6b, 7b, 8b, 9b, and 10b, the white lines indicate

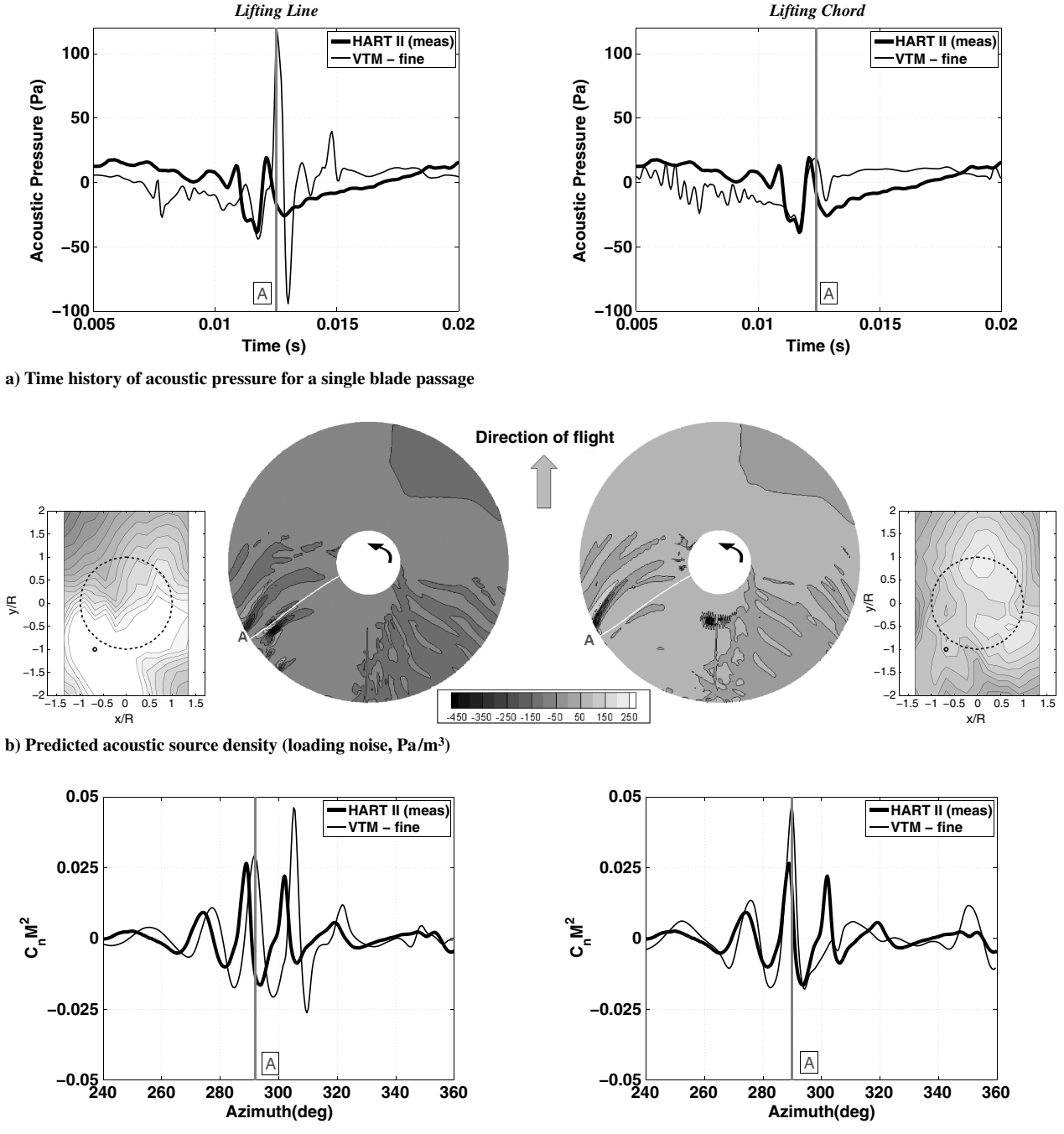


a) Time history of acoustic pressure for a single blade passage

b) Predicted acoustic source density (loading noise, Pa/m$^3$)

c) BVI-induced airloads

**Fig. 14 Time history of acoustic pressure for one blade passage and the corresponding BVI-induced airloads and source density distribution on the rotor for an observer (marked by small circle) located at the experimentally measured SPL maximum on the retreating side of the rotor (HART II MN case). Numerical results are for the fine computational resolution.**

the locus of sources at the time of several of the stronger acoustic features in the numerical predictions of the noise produced by the rotor. These loci can be used to identify the positions of the BVI events that are responsible for the corresponding acoustic feature, as is done in Figs. 5c, 6c, 7c, 8c, 9c, and 10c.

### 1. *Baseline HART II Flight Case*

In general, for the BL case, the computations reproduce the BVI acoustic signature at the microphone on the retreating side of the rotor with the correct phase, but the amplitude of several of the acoustic peaks is very sensitive to the grid resolution and to the aerodynamic model that is used to represent the blade airloads. The lifting-chord model more accurately captures the phase of the signal, and the accuracy of the prediction is influenced to a lesser extent by reducing the cell size than when the lifting-line model is used. The measured acoustic signature at this microphone contains a group of three peaks that occur at observer times of 0.011, 0.012, and 0.014 s, respectively. The most prominent numerically predicted acoustic features are marked as A and B in Figs. 5a, 5b, 6a, 6b, 7a, and 7b. The most intense feature (marked A in Figs. 5–7) is the result of the strong parallel BVI, which occurs at a blade azimuth of about 300°. It is interesting to note that the lifting-chord model predicts this intense BVI to occur about 2° earlier than when the lifting-line model is used (Figs. 5c, 6c, and 7c ). This shift is entirely consistent with the differences in implementation of the zero-throughflow boundary condition between the two models [22], and it may account for the consistent azimuthal discrepancy in the location of the SPL

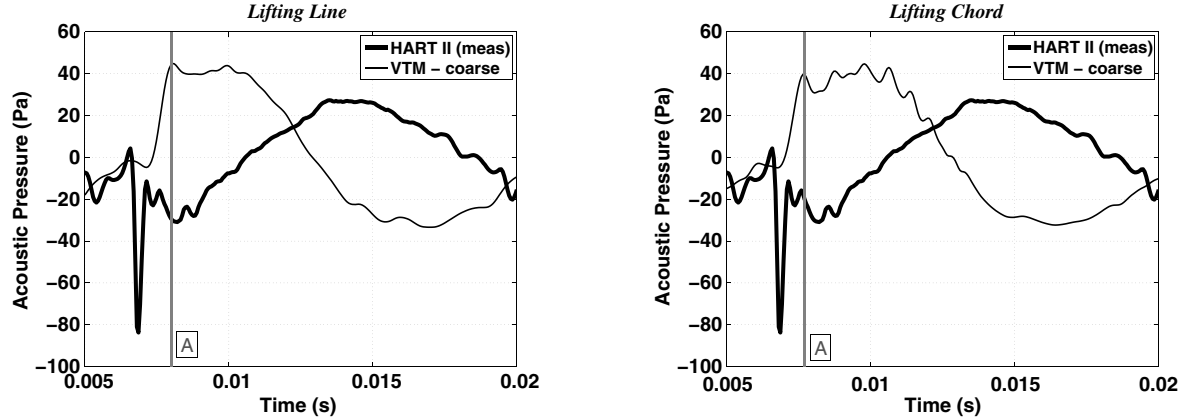


**a) Time history of acoustic pressure for a single blade passage**

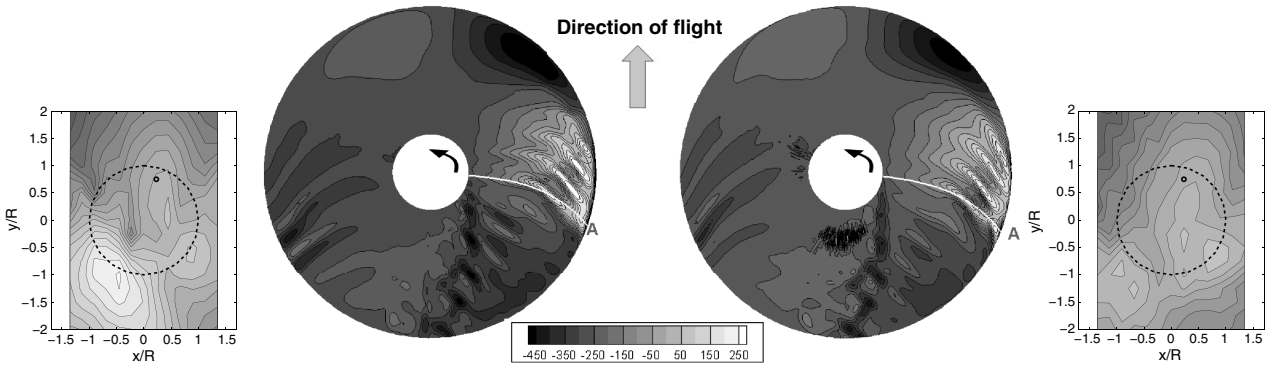


**b) Predicted acoustic source density (loading noise, Pa/m$^3$)**

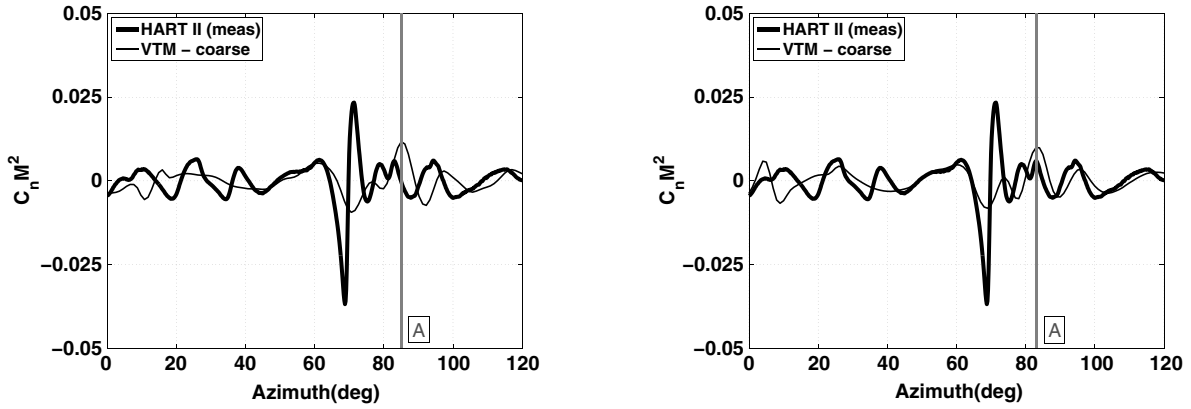


**c) BVI-induced airloads**

**Fig. 15 Time history of acoustic pressure for one blade passage and the corresponding BVI-induced airloads and source density distribution on the rotor for an observer (marked by small circle) located at the experimentally measured SPL maximum on the advancing side of the rotor (HART II MN case). Numerical results are for the coarse computational resolution.**

maximum on this side of the disk that is predicted by the two approaches. The reason for the rather obviously missing peak in the numerically generated acoustic signal at an observer time of 0.01 s remains obscure, but the appearance (or not) of certain features in the acoustic signature is known to be crucially dependent, on occasion, on the relative amplitude and phasing of several consecutive BVI events. The reason for this discrepancy may thus be difficult to localize.

The measured time history of acoustic pressure at the microphone located on the advancing side of the rotor disk is characterized by two strong acoustic pulses per blade passage (see Figs. 8a, 8b, 9a, 9b, 10a, and 10b), the stronger of which occurs at an observer time of approximately 0.016 s. The computations reproduce the BVI noise signature at this location reasonably well, but there is a consistent error in phase between the numerical and measured data. The amplitude of the predicted acoustic peaks is also very sensitive to the resolution of the flowfield, no matter which blade model is used.

In the BL case, the predicted airload shows generally good agreement with the measured signal, but the strongest BVI event on the advancing side of the disk is slightly misrepresented by the numerical method. In the measured signal, the loading peak with the largest amplitude occurs at approximately 50° azimuth. In contrast, the numerical calculations using both medium and fine grid resolutions predict the BVI event that occurs at an azimuth of 40° to be marginally stronger than the BVI at 50°. The predicted loading intensity is thus shifted toward the rear of the disk compared with the experiment. At the finest computational resolution, the difference in magnitude between each of these two BVI impulses is, however,

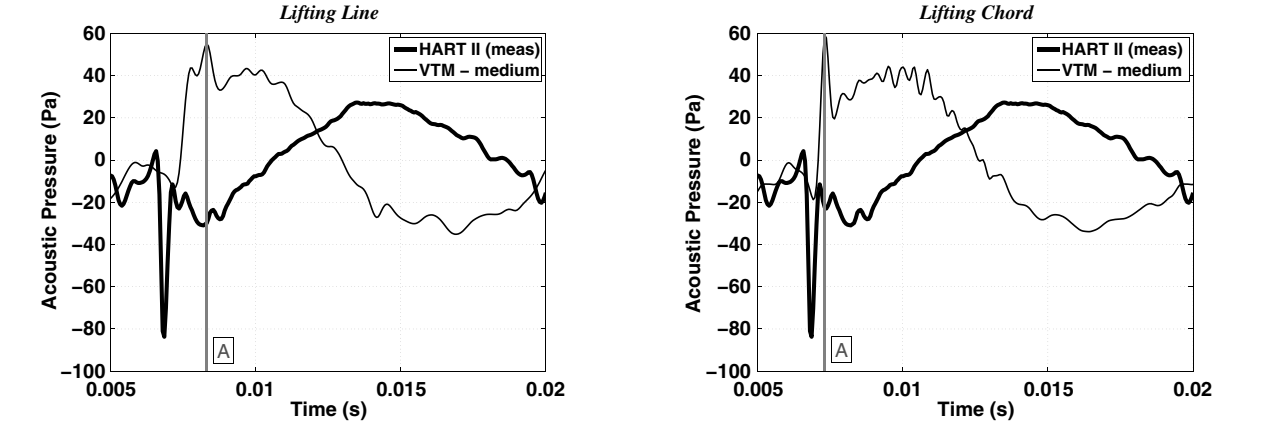


a) Time history of acoustic pressure for a single blade passage

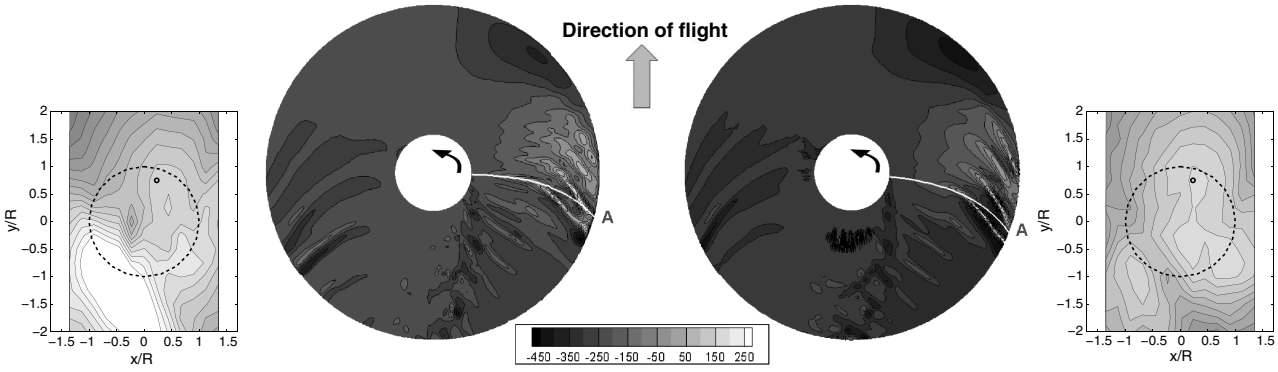


b) Predicted acoustic source density (loading noise, Pa/m$^3$)

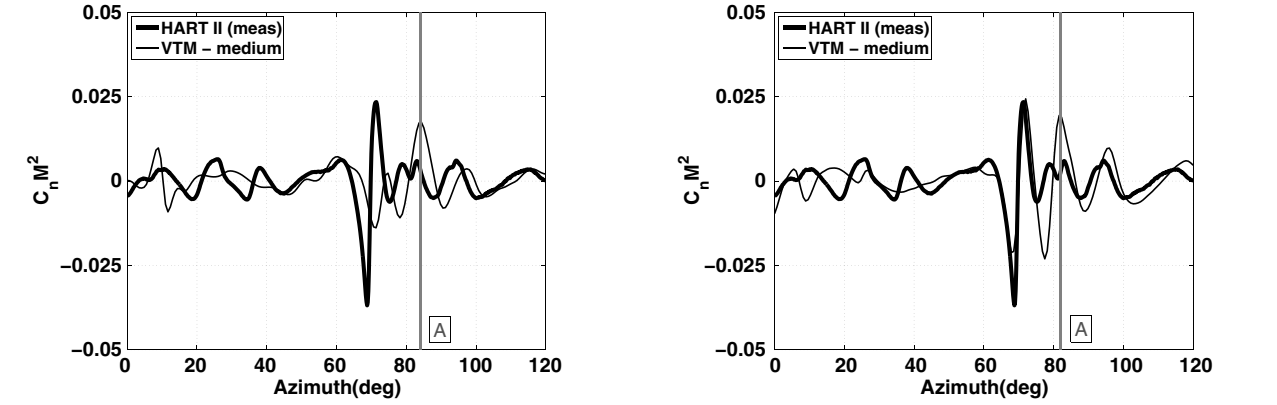


c) BVI-induced airloads

**Fig. 16 Time history of acoustic pressure for one blade passage and the corresponding BVI-induced airloads and source density distribution on the rotor for an observer (marked by small circle) located at the experimentally measured SPL maximum on the advancing side of the rotor (HART II MN case). Numerical results are for the medium computational resolution.**

minimal. It is believed that this sensitivity in the relative strength of these BVIs to the computational resolution has a strong influence on the predicted position of the acoustic maximum on the advancing side of the disk. The principal peak in the predicted acoustic signature at the maximum on the advancing side of the rotor is associated with a BVI event on this side of the disk, which occurs when the reference blade is located at approximately 40° azimuth (marked A in Figs. 8–10). Figure 11 shows the geometry of the wake at this instant and reveals the root vortices that are extruded from blades 1, 2, and 3, as well as a relatively old tip vortex from blade 4, interacting strongly with the reference blade. However, there is some question as to the accuracy of the representation of the root vortex system. Given the absence of any model of the rotor hub assembly in the simulations, any error in the prediction of the strength of the vorticity trailed from the roots of the blade would adversely affect the predictions of the flow, and hence the predictions of acoustic pressure that are generated by the blades as they pass near the rear of the disk. An overly strong root vortex structure could quite feasibly distort the trajectories of the tip vortices that are responsible for the BVIs as they pass upward and through the zones of maximum BVI activity on the rotor disk or, indeed, combine with the vorticity in the interacting vortex, resulting in an overprediction of the intensity of the interaction. A parametric study has shown, however, that very little qualitative improvement in the blade loading is obtained by varying the boundary condition that is applied at the root of the blade, and hence the strength of the vortices that originate from there.

In all cases, the predominant peak in the acoustic signal at the maximum on the advancing side of the rotor occurs later in the

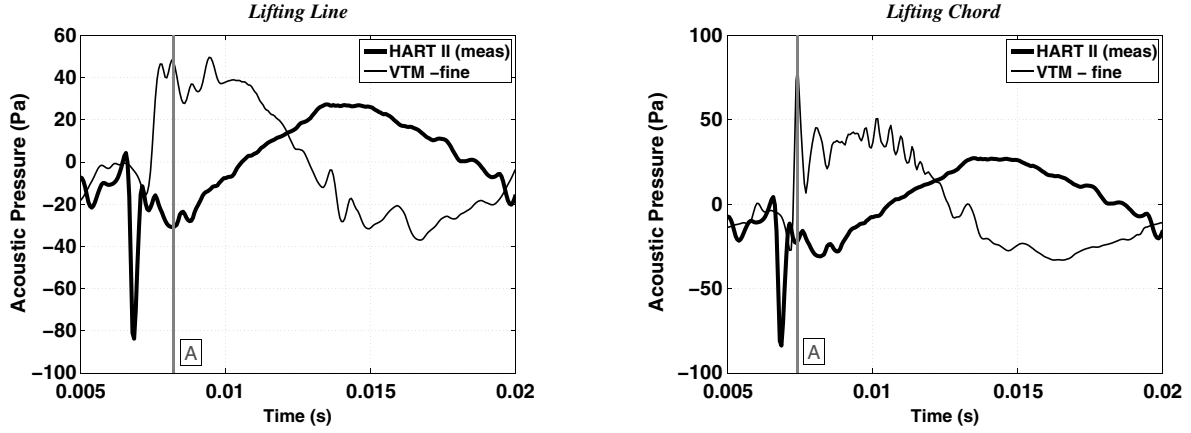


a) Time history of acoustic pressure for a single blade passage

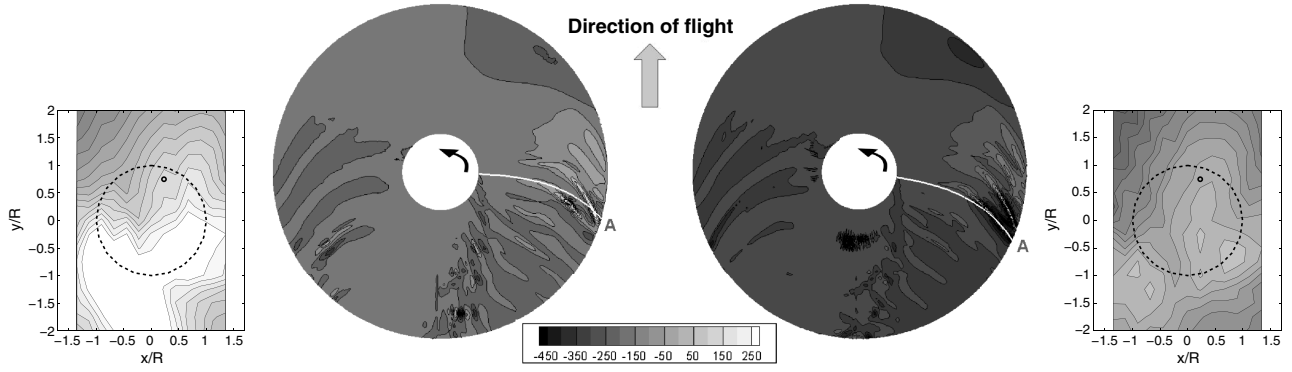


b) Predicted acoustic source density (loading noise, Pa/m$^3$)

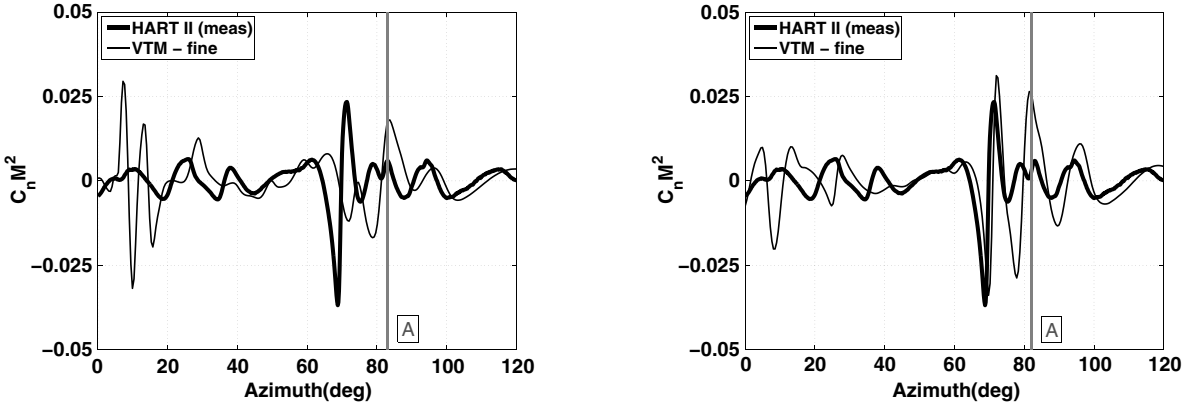


c) BVI-induced airloads

**Fig. 17 Time history of acoustic pressure for one blade passage and the corresponding BVI-induced airloads and source density distribution on the rotor for an observer (marked by small circle) located at the experimentally measured SPL maximum on the advancing side of the rotor (HART II MN case). Numerical results are for the fine computational resolution.**

simulations than in the experimental data, indeed suggesting that at least a small misplacement of the vortex might be responsible for the discrepancies in the numerical representation of this acoustic feature.

*2. Minimum-Noise HART II Flight Case*

Figures 12–17 show similar data to Figs. 5–10 but for the HART II MN flight case. Predicted and measured time histories of acoustic pressure at the positions of the two microphones located at the points of measured maximum noise level on the advancing and retreating sides of the rotor (microphones M8 and M4, respectively), are shown in Figs. 12a, 13a, 14a, 15a, 16a, and 17a. As in the BL case, for the MN case, the BVI acoustic signature at the microphone on the retreating side of the rotor is much better predicted by the computations than that on the advancing side of the disk. The dominant acoustic peak on the retreating side occurs at an observer time of 0.012 s (marked as A in Figs. 12–14) and is generally predicted with the correct phase and amplitude if the lifting-chord model is used to represent the aerodynamics of the rotor blades, regardless of the resolution of the computation. Where the lifting-line model is used, the amplitude of this acoustic peak is very sensitive to the grid resolution and, as a result, the model consistently overpredicts the acoustic maximum on this side of the disk. Although the phase of the signal is generally well predicted by the lifting-line model, it is more accurately captured by the lifting-chord model. This is most likely due to the differences between the two aerodynamic models in their predictions of the position of the most intense BVI on the retreating side of the rotor. Figures 12c, 13c, and 14c show that, in the predictions of the lifting-chord model and, indeed, in the experimental data, the strongest BVI event occurs at 290° azimuth. The lifting-line model consistently overpredicts the BVI-induced peak at 305° azimuth; thus, this BVI becomes the dominant peak in the airload predictions where this model has been used in the calculations. Although the earlier BVI event at 290° azimuth is not the main contributor to the noise produced at the acoustic maximum on the retreating side of the rotor, it is likely that the relative strength of the two BVI events that occur between 280 and 310° affect the phasing of the corresponding acoustic features that are produced on this side of the rotor disk.

On the advancing side of the rotor disk, the discrepancies between the measured time history of acoustic pressure and the signal that is predicted by the VTM are much larger. The experimental signal is characterized by a strong negative peak at an observer time of approximately 0.007 s (marked A in Figs. 8a, 8b, 9a, 9b, 10a, and 10b). Although this feature is clearly reproduced in the predicted signal, there are errors in both phasing and amplitude at all computational resolutions and using both blade aerodynamic models. It is therefore not surprising that it is the acoustic maximum on this side of the rotor disk in this flight case that is the least well predicted of all the cases that have been simulated. Indeed, this observation is also consistent with those made regarding the predictions of the high-frequency blade airloads for the MN case, which show the largest errors in phase and amplitude for this flight case, irrespective of the computational resolution or the blade model that has been used.

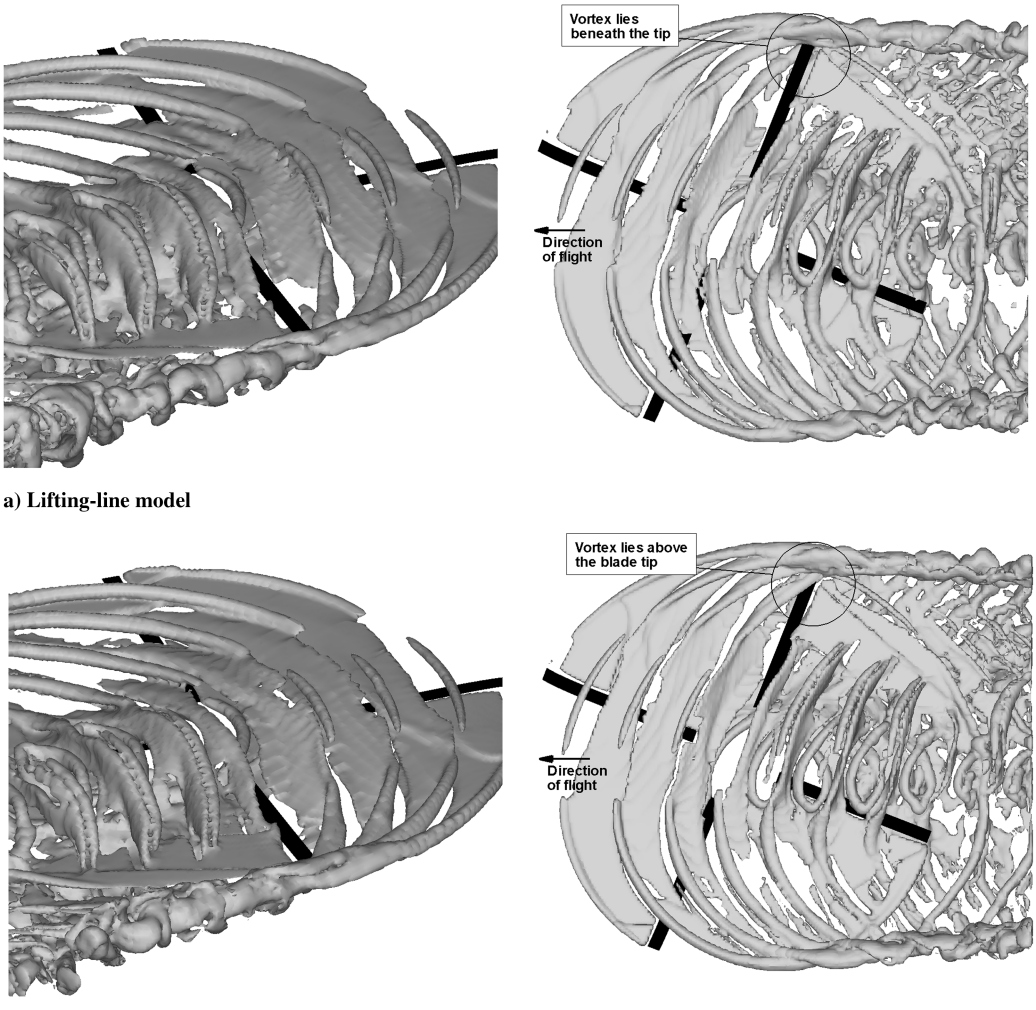


**Fig. 18 Geometry of the BVI at 70° azimuth, as predicted using lifting-line and lifting-chord representations of the blade aerodynamics, for the HART II MN flight case (medium computational resolution).**

In the MN case, the most intense BVI impulse found in the blade airloads, at an azimuth of 70° on the advancing side, is underpredicted in amplitude when the lifting-line model is used, regardless of the resolution of the flowfield. In contrast, as the grid resolution is increased, the lifting-chord model very accurately captures this particular loading peak.

Figure 18 compares the wake structure that is predicted by the VTM at the medium resolution for the MN case when the lifting-chord representation of the aerodynamics of the blade is used to that predicted when the lifting-line model is used. This figure shows the sensitivity of the predicted wake structure to the model that is used to represent the blade aerodynamics. In the calculation in which the lifting-line model has been used, the vortex that is responsible for the most prominent BVI in the MN case passes beneath the blade, whereas when the lifting-chord model is used, the vortex passes above the blade. It has been shown previously that the VTM-predicted airloads are sensitive to the very subtle changes in the vorticity distribution that is sourced into the flow by the blades when different blade aerodynamic models are used; in this case, given the shallow angle between the vortex and the blade, it can easily be conceived how a small change in the predicted position of the vortex could have a large effect on the predictions of the associated BVI airload.

Increasing the computational resolution somewhat increases the accuracy of the predictions of the BVI features in the acoustic pressure where the lifting-chord model has been used to represent the aerodynamics of the rotor blades within the computation. As a result, the SPL maximum on the advancing side shows the most favorable

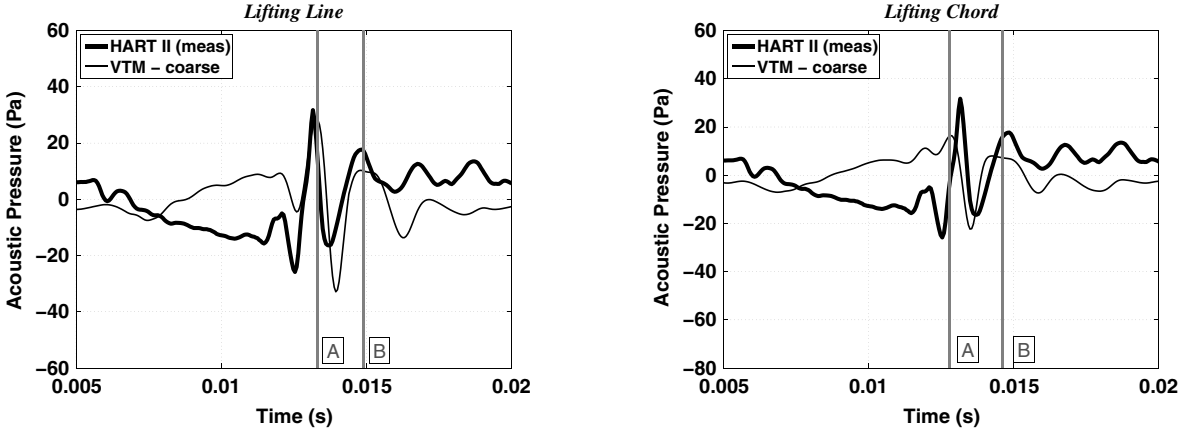


a) Time history of acoustic pressure for a single blade passage

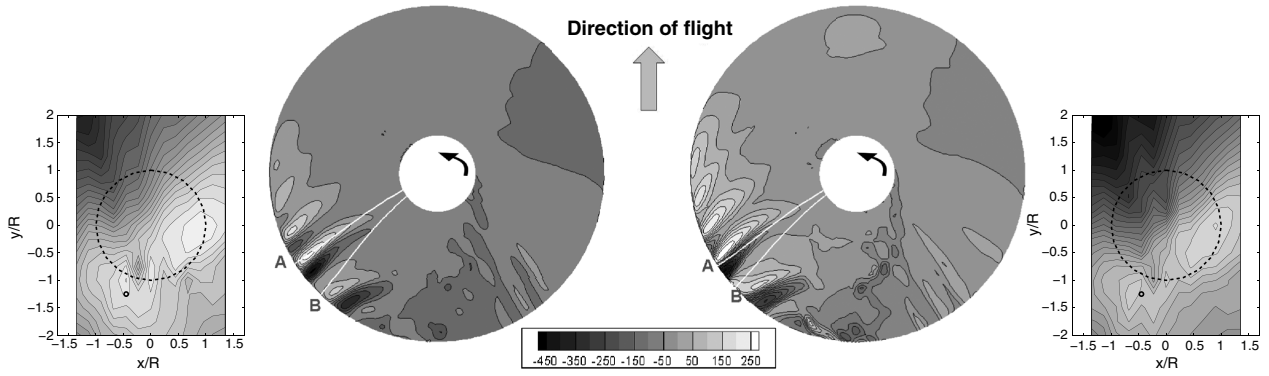


b) Predicted acoustic source density (loading noise, Pa/m$^3$)

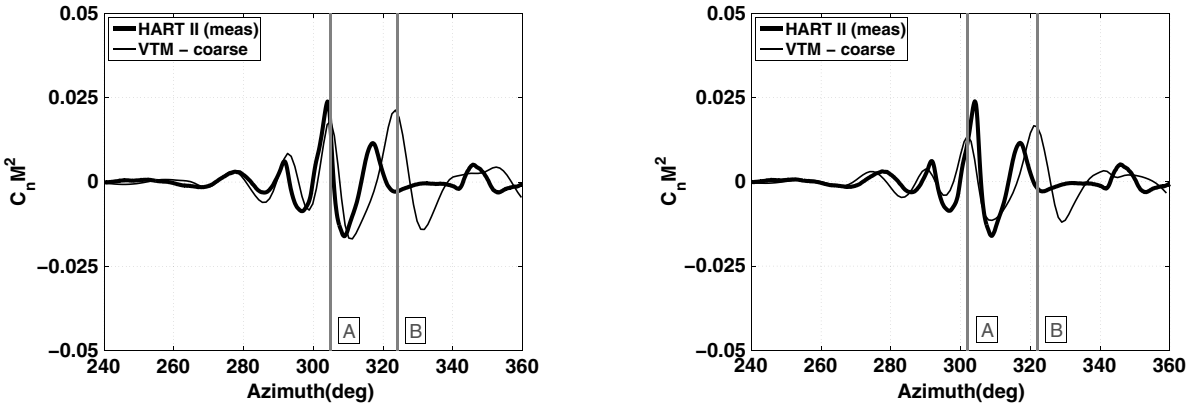


c) BVI-induced airloads

**Fig. 19 Time history of acoustic pressure for one blade passage and the corresponding BVI-induced airloads and source density distribution on the rotor for an observer (marked by small circle) located at the experimentally measured SPL maximum on the retreating side of the rotor (HART II MV case). Numerical results are for the coarse computational resolution.**

correlation with the measured data when predicted using the lifting-chord model at the fine computational resolution.

### 3. *Minimum-Vibration HART II Flight Case*

Figures 19–24 compare the predicted and measured time histories of acoustic pressure at the positions of the two microphones located at the points of measured maximum noise level on the advancing and retreating sides of the rotor for the MV case (microphones M10 and M5, respectively). On the retreating side of the disk, the time history of acoustic pressure is very similar to that of the BL flight case, which is not surprising, given that the geometry of the wake and, in particular, the position and intensity of the BVI events on this side of the rotor are very similar in both cases. The two principal peaks in the MN case occur at observer times of approximately 0.013 and 0.015 s and are marked as A and B in Figs. 19a, 20a, and 21a. The plots of acoustic density (Figs. 19b, 20b, and 21b) show two very strong BVI events in the fourth quadrant of the rotor disk. The interaction that produces the most impulsive acoustic feature occurs at a blade azimuth of about 310° and, in a similar way to that in the BL case, is most likely due to a near-parallel BVI. Again, the predicted acoustic pressure shows a marked improvement in comparison with experimental data when the lifting-chord model has been used to represent the aerodynamic is the blades. This is because this model more accurately predicts the phase and the amplitude of the acoustic features that are present compared with the lifting-line model.

The time history of the acoustic pressure on the advancing side of the disk is much more complicated. The measured signal is

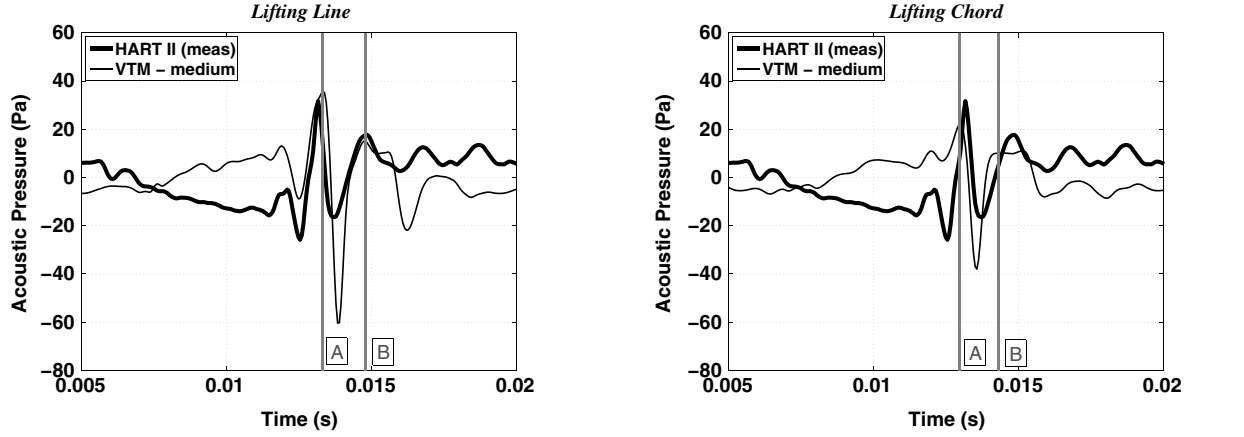


**a) Time history of acoustic pressure for a single blade passage**

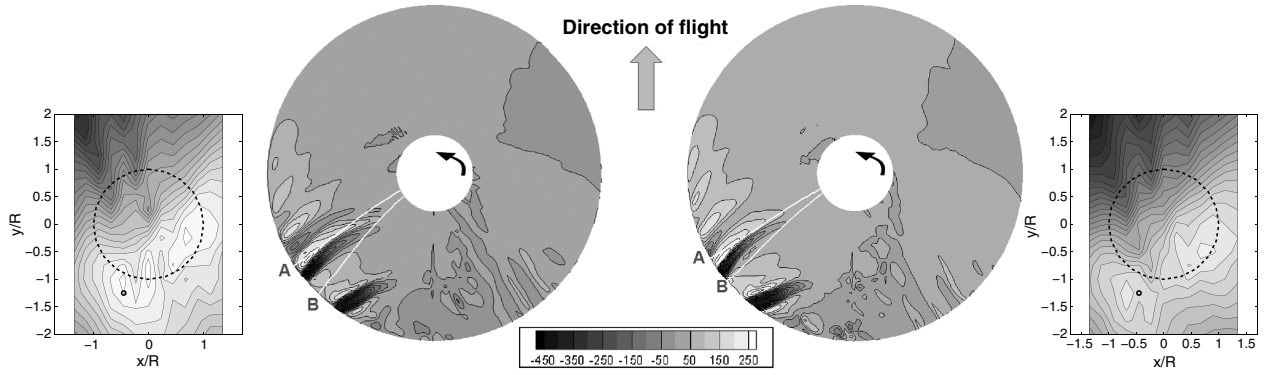


**b) Predicted acoustic source density (loading noise, Pa/m$^3$)**

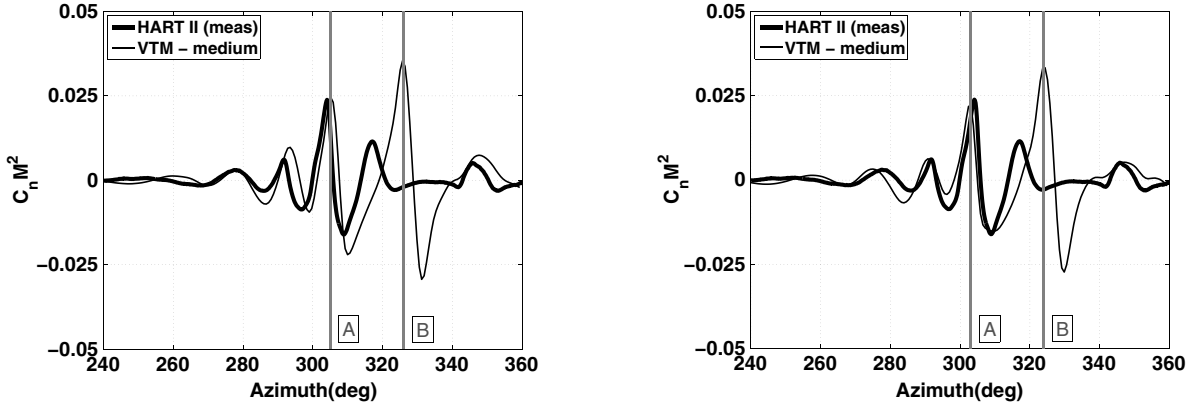


**c) BVI-induced airloads**

**Fig. 20 Time history of acoustic pressure for one blade passage and the corresponding BVI-induced airloads and source density distribution on the rotor for an observer (marked by small circle) located at the experimentally measured SPL maximum on the retreating side of the rotor (HART II MV case). Numerical results are for the medium computational resolution.**

dominated by three strong peaks at observer times of 0.014, 0.015, and 0.016 s, respectively. Although similar peaks are apparent in the numerically predicted signal, there are large discrepancies in the phase and amplitude of these acoustic features. The observed features correspond to fairly similar BVI-induced loading peaks at blade azimuths of 23, 35, and 45°, as shown in Figs. 22c, 23c, and 24c, each having much the same amplitudes and pulse widths. Correspondingly, the measured acoustic signal also contains three principal acoustic peaks, each of similar pulse width and amplitude. In the predicted BVI-induced airloads, a consistent phase shift relative to the measured data results in an error in the predicted phase of the acoustic pressure signal and, ultimately, in a slight error in the prediction of the SPL maximum on this side of the rotor disk. In addition to the BVI events that are observed in the plots of acoustic source density, the ridge that is visible in the contours in the second quadrant of the rotor disk is worthy of note. This is most likely due to the reversed loading at the tip of the advancing blade under the conditions of this particular test, which causes the formation of a twin vortex structure on this side of the rotor. However, this feature, although interesting, is not thought to contribute significantly to the acoustic radiation from the rotor.

## V. Conclusions

Aerodynamic and acoustic predictions using Brown's VTM are compared against the HART II wind tunnel data for an experimental model based on the characteristics of the main rotor of the Bo105 helicopter. The rotor was flown in a descending flight condition in

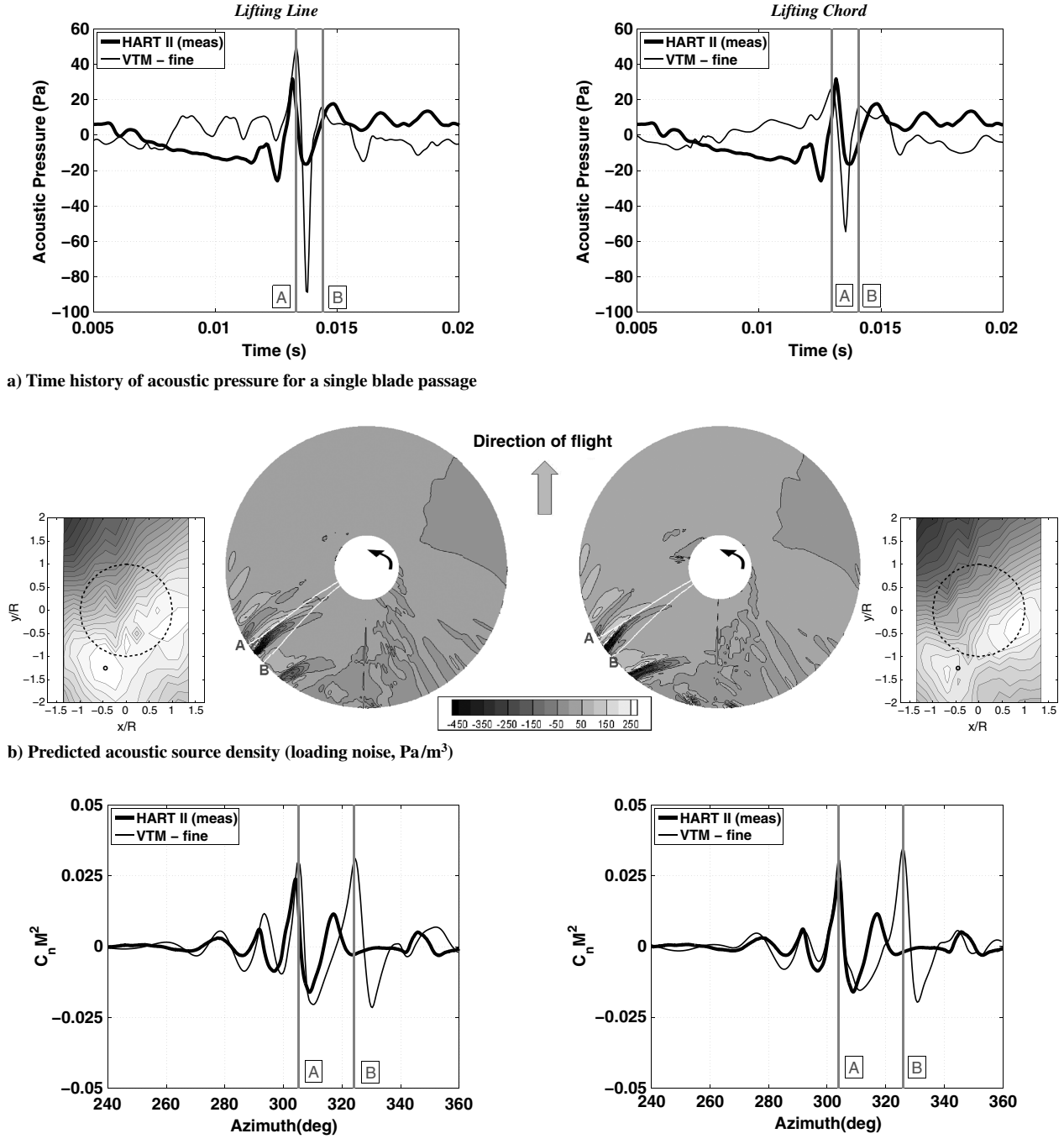


a) Time history of acoustic pressure for a single blade passage

b) Predicted acoustic source density (loading noise, Pa/m$^3$)

c) BVI-induced airloads

**Fig. 21 Time history of acoustic pressure for one blade passage and the corresponding BVI-induced airloads and source density distribution on the rotor for an observer (marked by small circle) located at the experimentally measured SPL maximum on the retreating side of the rotor (HART II MV case). Numerical results are for the fine computational resolution.**

which the loading on its blades contained significant high-frequency content due to the presence of BVIs. These data have been used in the present paper to analyze the ability of two blade aerodynamic models to capture the detailed high-frequency BVI-induced loading on the rotor, and thus the acoustic signature of the helicopter. The first model is an extension of the Weissinger-L lifting-line model, in which the strength of a bound vortex, placed at the quarter-chord of each blade panel, is determined by imposing a zero-throughflow boundary condition at a single point located at the three-quarter-chord of the panel. This approach is compared with a second lifting-chord method that is based on classical unsteady thin aerofoil theory. In this approach, the aerodynamic environment of the blade is represented by a series of weighted integrals over the chord of each blade panel. The version of the model that was used includes a prescription of the blade dynamics that is derived from the HART II experimental data.

The predicted airload for all three HART II flight cases compares very favorably with the experimentally measured airloads. On the retreating side of the rotor, all BVI events discernible in the experimental data are reproduced by the numerics, usually with the correct phase. Generally on the advancing side of the rotor, the numerical resolution of the BVI-induced loads is less accurate in both amplitude and phase, yet all BVIs seen in the experimental data are still captured. For the MN and MV cases, both blade models have been shown to accurately capture the shifts in position of the BVI events on the rotor that result from the application of HHC.

Three computational resolutions were used to expose the effect of grid resolution on the quality of predictions. Where the lifting-line

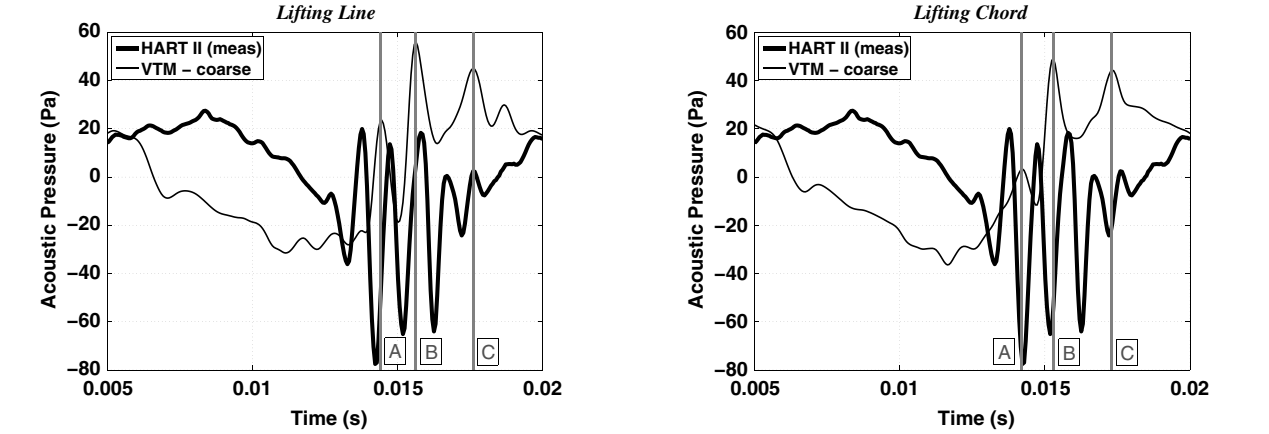


a) Time history of acoustic pressure for a single blade passage

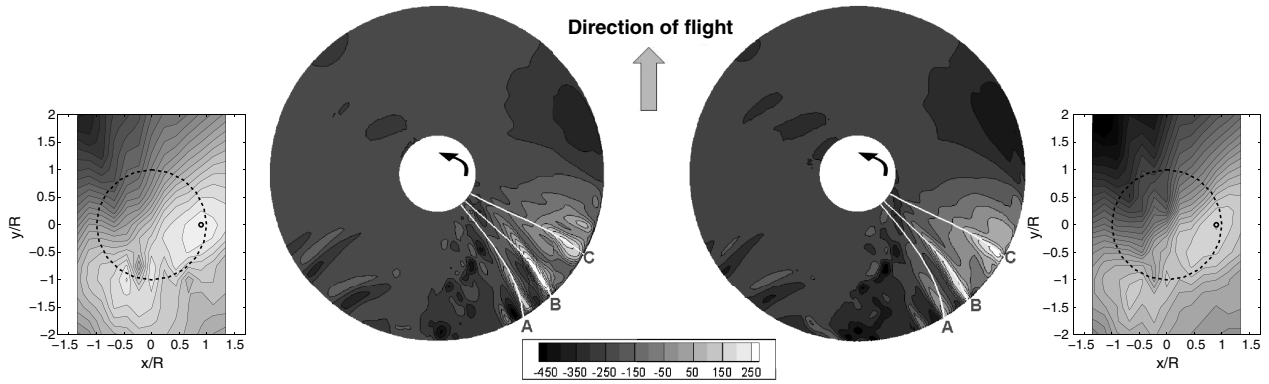


b) Predicted acoustic source density (loading noise, Pa/m$^3$)

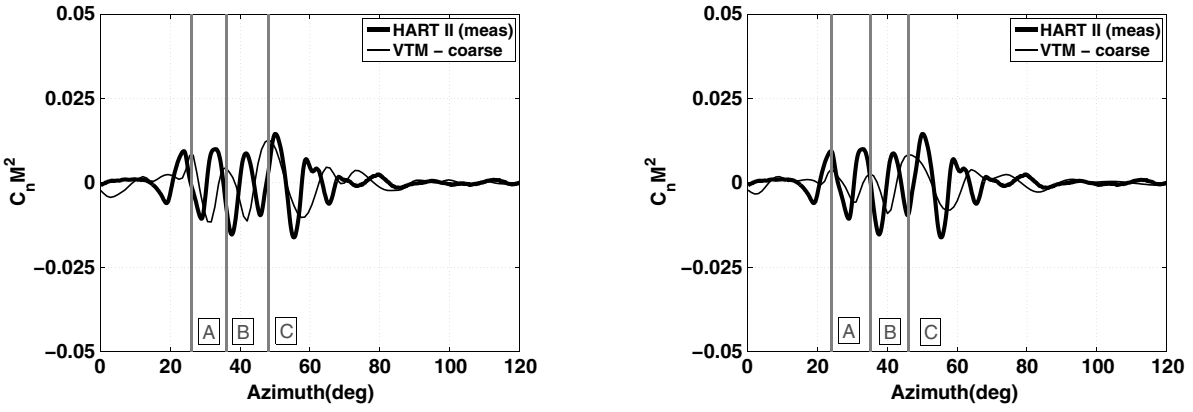


c) BVI-induced airloads

**Fig. 22 Time history of acoustic pressure for one blade passage and the corresponding BVI-induced airloads and source density distribution on the rotor for an observer (marked by small circle) located at the experimentally measured SPL maximum on the advancing side of the rotor (HART II MV case). Numerical results are for the coarse computational resolution.**

model was used to represent the aerodynamics of the blades, the predicted high-frequency BVI-induced component of the loading is found to be extremely sensitive to the cell size that is used in the computations. The predicted amplitude of the BVI-induced features in the loading on the blades increases significantly as the cell size that is used to resolve the wake is reduced. A marked improvement in the accuracy of the predicted high-frequency airloads of the HART II rotor is obtained when a lifting-chord model for the blade aerodynamics is used instead of the lifting-line-type approach. Errors in the amplitude and phase of the BVI-loading peaks are reduced, and the quality of the prediction is affected to a lesser extent by the computational resolution. In particular, the overprediction of the amplitude of the BVI events, which occurs on the retreating side of the disk as the resolution of the computation is increased when using the lifting-line model, is avoided.

Similar conclusions extend to the predicted acoustic signature of the rotor. The experimentally measured directivity of the radiated noise pattern is generally well captured by the numerics, as is the location and magnitude of the maxima in the SPL on the measurement plane below the rotor, at least on the retreating side of the disk. The upstream decay of the radiated signal is also well captured, particularly in the BL test case. Yet again, the larger deficiencies in prediction are encountered on the advancing side of the rotor, where magnitude and phase errors in the predicted BVI-induced component of the blade loading translate into more significant errors in the position and magnitude of the maximum in the sound pressure field on this side of the rotor than on the retreating side.

The time history of the acoustic pressure at the SPL maximum on each side of the disk is used to determine the time of several of the stronger acoustic features in the numerical predictions. Loci of

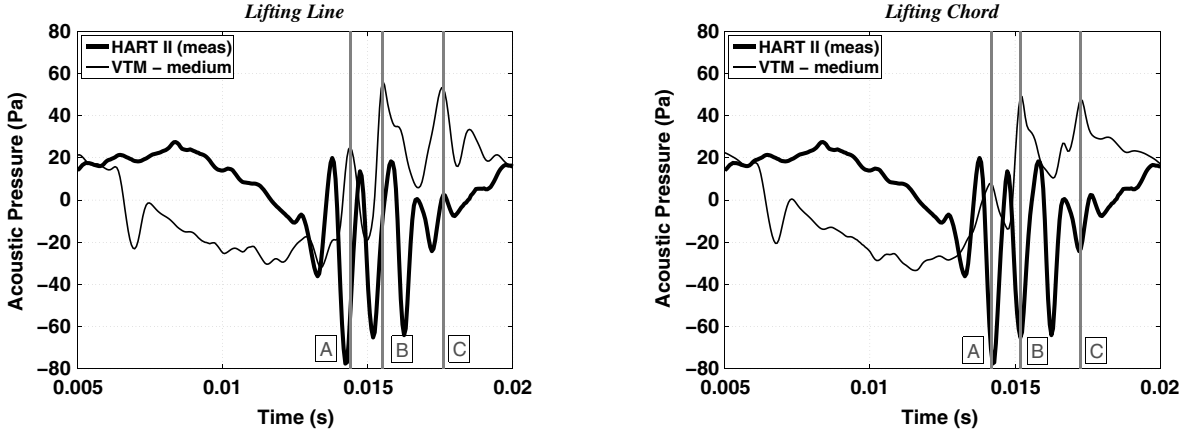


a) Time history of acoustic pressure for a single blade passage

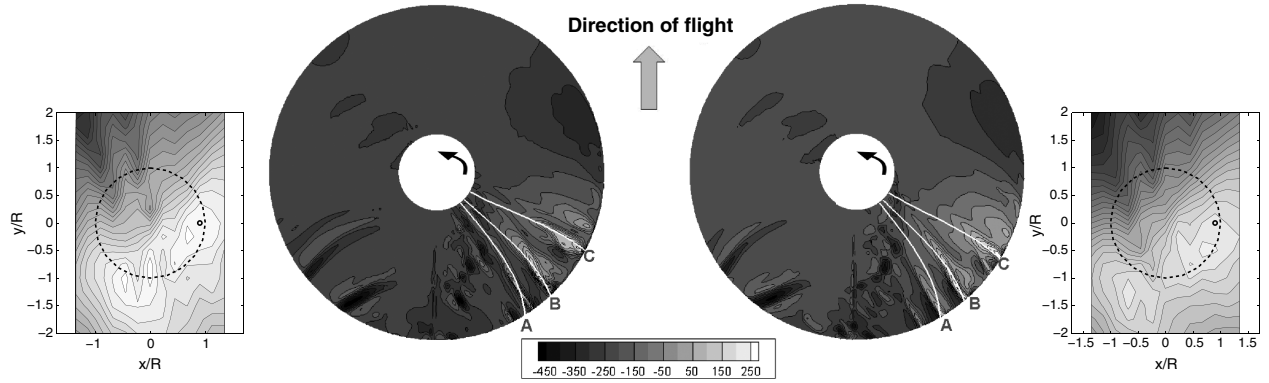


b) Predicted acoustic source density (loading noise, Pa/m$^3$)

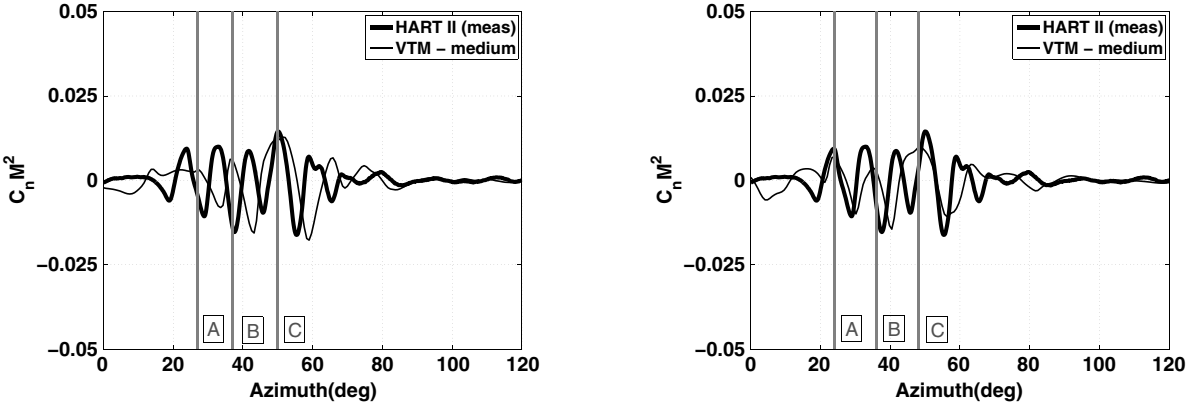


c) BVI-induced airloads

**Fig. 23 Time history of acoustic pressure for one blade passage and the corresponding BVI-induced airloads and source density distribution on the rotor for an observer (marked by small circle) located at the experimentally measured SPL maximum on the advancing side of the rotor (HART II MV case). Numerical results are for the medium computational resolution.**

sources at the observer times when the stronger acoustic features occur are plotted on the predicted distribution of acoustic source density, and they are used to determine the positions on the rotor disk of the major acoustic sources. The principal features in the acoustic pressure signal can then be tracked back to the individual BVI-loading peaks in the airload predictions.

Where the lifting-line model was used to represent the aerodynamics of the blades, the resulting time history of the acoustic pressure that is predicted is found to be extremely sensitive to the cell size that is used in the computations. The predicted amplitude of the BVI-induced acoustic features increases significantly as the cell size that is used to resolve the wake is reduced. The overprediction of the amplitude of the BVI-induced acoustic features is less apparent when using the lifting-chord model. While the blade airload is less sensitive to maxima and minima in the velocity profile when using the lifting-chord approach, the acoustic postprocessing method depends on the loading gradients rather than directly on the amplitude of the BVI-loading peaks, and it is therefore more sensitive. In almost all cases, however, increasing the resolution of the computational grid increases the accuracy of the acoustic predictions when the lifting-chord model is used; thus, the lifting-chord model at the highest resolution produces the best representation of the distribution of sound pressure below the rotor.

Nevertheless, the results presented here suggest that further improvements in blade aerodynamic modeling or further increases in spatial resolution are unlikely to produce concomitant improvements in the prediction of the acoustic signature of the helicopter when using the class of methods described in this paper. Instead,

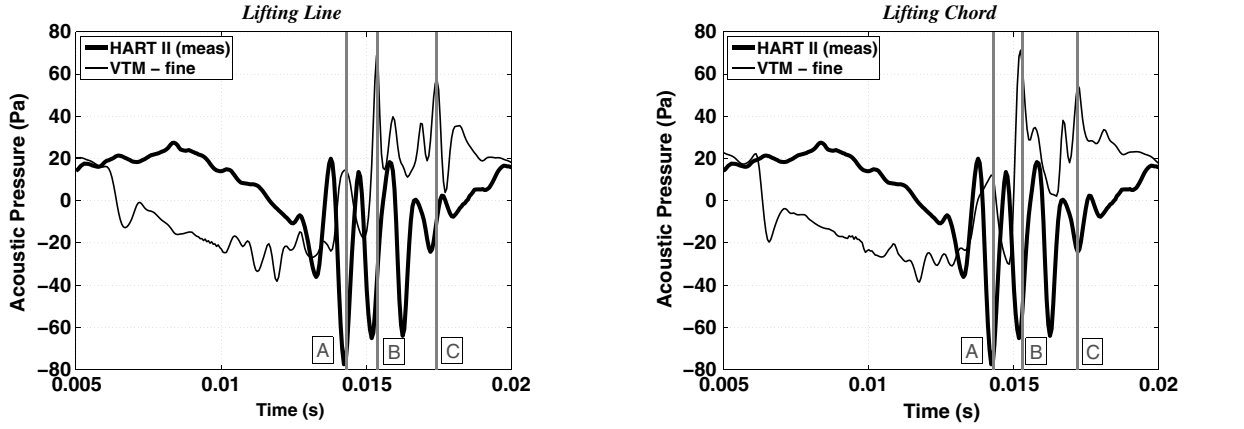


a) Time history of acoustic pressure for a single blade passage

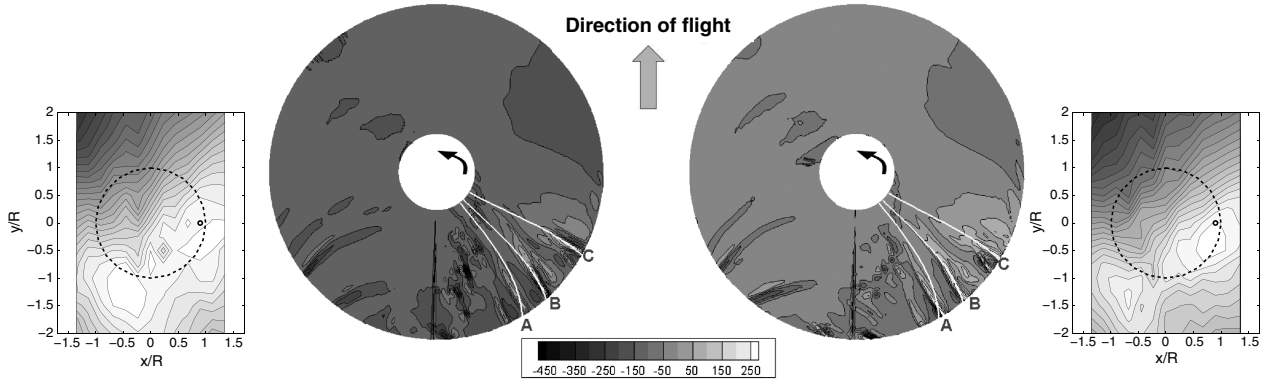


b) Predicted acoustic source density (loading noise, Pa/m$^3$)

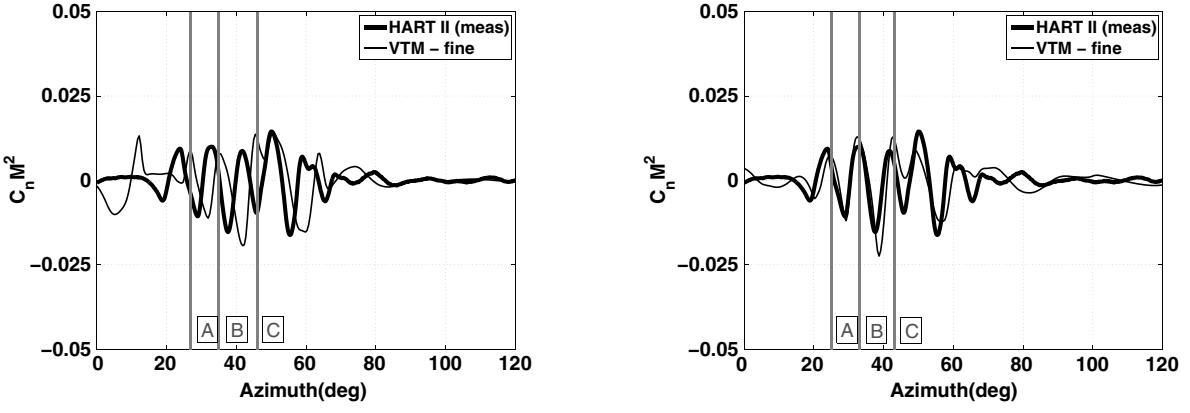


c) BVI-induced airloads

**Fig. 24 Time history of acoustic pressure for one blade passage and the corresponding BVI-induced airloads and source density distribution on the rotor for an observer (marked by small circle) located at the experimentally measured SPL maximum on the advancing side of the rotor (HART II MV case). Numerical results are for the fine computational resolution.**

fundamental improvements in the formulation of the approach are required so that the physical processes occurring within the wake, rather than the size of the computational cells, are responsible for setting the fundamental lower limit on the size of the smallest vortical structures that can be resolved within the computational domain. To this end, future work will concentrate on resolving the viscous and turbulent processes that are responsible for the internal detail (particularly, the growth in spatial extent) of the vortical structures within the rotor wake.

## Acknowledgments

The authors would like to thank the members of the Higher-Harmonic Control Aeroacoustics Rotor Test team for providing the data that were used in this study. In particular, the authors would like to thank Berend van der Wall and Joon Lim for their useful comments during the course of the research leading to this paper. The authors would also like to thank Jay Sitaraman and Karthik Duraisamy, authors of the acoustic postprocessor used in this study.

## References

[1] van der Wall, B. G., Junker, B., Burley, C., Brooks, T., Yu, Y. H., Tung, C., Raffel, M., Richard, H., Wagner, W., Mercker, E., Pengel, K., Holthusen, H., Beaumier, P., and Delrieux, Y., "The HART II Test in the LLF of the DNW: A Major Step Towards Rotor Wake Understanding," *Proceedings of the 28th European Rotorcraft Forum* [CD-ROM], Bristol, England, Royal Aeronautical Soc., London, 2002.

[2] van der Wall, B. G., Burley, C., Yu, Y. H., Richard, H., Pengel, K., and Beaumier, P., "The HART II Test-Measurement of Helicopter Rotor Wakes," *Aerospace Science and Technology*, Vol. 8, No. 4, 2004, pp. 273–284. doi:10.1016/j.ast.2004.01.001

[3] Lim, J. W., Tung, C., Yu, Y. H., Burley, C., Brooks, T., Boyd, D., van der Wall, B. G., Schneider, O., Richard, H., Raffel, M., Beaumier, P., Delrieux, Y., Pengel, K., and Mercker, E., "HART II: Prediction of Blade–Vortex Interaction Loading," *Proceedings of the 29th European Rotorcraft Forum* [CD-ROM], Friedrichshafen, Germany, German Society for Aeronautics and Astronautics, Cologne, Germany, 2003.

[4] Yu, Y. H., Tung, C., van der Wall, B. G., Pausder, H., Burley, C., Brooks, T., Beaumier, P., Delrieux, Y., Mercker, E., and Pengel, K., "The HART-II Test: Rotor Wakes and Aeroacoustics with Higher-Harmonic Pitch Control (HHC) Inputs: The Joint German/French/Dutch/U.S. Project," *Proceedings of the American Helicopter Society 58th Annual Forum* [CD-ROM], Montreal, American Helicopter Soc., Washington, D.C., 2002.

[5] Boyd, D. D., "HART II Acoustic Predictions Using a Coupled CFD/CSD Method," *Proceedings of the American Helicopter Society 65th Annual Forum* [CD-ROM], Grapevine, TX, American Helicopter Soc., Washington, D.C., 2009.

[6] Lim, J. W., Nygaard, T., Strawn, R., and Potsdam, M., "BVI Airloads Prediction Using CFD/CSD Loose Coupling," *Proceedings of the AHS Specialists' Meeting on Vertical Lift Design Conference* [CD-ROM], San Francisco, CA, American Helicopter Soc., Washington, D.C., 2006.

[7] Lim, J. W., and Strawn, R. C., "Prediction of HART II Rotor BVI Loading and Wake System Using CFD/CSD Loose Coupling," 45th AIAA Aerospace Sciences Meeting and Exhibit, Reno, NV, AIAA Paper 2007-1281, 2007.

[8] Whitehouse, G., Boschitsch, A., Quackenbush, T., Wachspress, D., and Brown, R. E., "Novel Eulerian Vorticity Transport Wake Module for Rotorcraft Flow Analysis," *Proceedings of the American Helicopter Society 63rd Annual Forum* [CD-ROM], Virginia Beach, VA, American Helicopter Soc., Washington, D.C., 2007.

[9] Kelly, M. E., Duraisamy, K., and Brown, R. E., "Predicting Blade–Vortex Interaction Airloads and Acoustics Using the Vorticity Transport Model," *Proceedings of the AHS 9th Specialists' Meeting on Aeromechanics* [CD-ROM], San Francisco, CA, American Helicopter Soc., Washington, D.C., 2008.

[10] Kelly, M. E., and Brown, R. E., "Predicting the Wake Structure of the HART II Rotor Using the Vorticity Transport Model," *Proceedings of the 34th European Rotorcraft Forum* [CD-ROM], Liverpool, U.K., Royal Aeronautical Soc., London, 2008.

[11] Kelly, M. E., and Brown, R. E., "The Effect of Blade Aerodynamic Modelling on the Prediction of High-Frequency Rotor Airloads," *Proceedings of the American Helicopter Society 65th Annual Forum* [CD-ROM], Grapevine, TX, American Helicopter Soc., Washington, D.C., 2009.

[12] Brown, R. E., and Line, A. J., "Efficient High-Resolution Wake Modeling Using the Vorticity Transport Model," *AIAA Journal*, Vol. 43, No. 7, 2005, pp. 1434–1443. doi:10.2514/1.13679

[13] Brown, R. E., "Rotor Wake Modeling for Flight Dynamic Simulation of Helicopters," *AIAA Journal*, Vol. 38, No. 1, 2000, pp. 57–63. doi:10.2514/2.922

[14] Toro, E. F., "A Weighted Average Flux Method for Hyperbolic Conservation Laws," *Proceedings of the Royal Society of London, Series A: Mathematical and Physical Sciences*, Vol. 423, No. 1865, 1989, pp. 401–418. doi:10.1098/rspa.1989.0062

[15] Peters, D. A., Hsieh, M.-C., and Torrero, A., "A State-Space Airloads Theory for Flexible Airfoils," *Journal of the American Helicopter Society*, Vol. 52, No. 4, 2007, pp. 329–342. doi:10.4050/JAHS.52.329

[16] Kenyon, A. R., and Brown, R. E., "Wake Dynamics and Rotor–Fuselage Aerodynamic Interactions," *Journal of the American Helicopter Society*, Vol. 54, No. 1, 2009, Paper 012003. doi:10.4050/JAHS.54.012003

[17] Schneider, O., "Analysis of SPR Measurements from HART II," *Aerospace Science and Technology*, Vol. 9, No. 5, 2005, pp. 409–420. doi:10.1016/j.ast.2005.01.013

[18] Schneider, O., van der Wall, B. G., and Pengel, K., "HART II Blade Motion Measured by Stereo Pattern Recognition (SPR)," *Proceedings of the American Helicopter Society 59th Annual Forum* [CD-ROM], Phoenix, AZ, American Helicopter Soc., Washington, D.C., 2003.

[19] Pengel, K., Müller, R., and van der Wall, B. G., "Stereo Pattern Recognition: The Technique for Reliable Rotor Blade Deformation and Twist Measurement," *Proceedings of the AHS International Meeting on Advanced Rotorcraft Technology and Life Saving Activities* [CD-ROM], Utsunomiya, Japan, American Helicopter Soc., Washington, D.C., 2002.

[20] Farassat, F., and Succi, G. P., "The Prediction of Helicopter Rotor Discrete Frequency Noise," *Vertica*, Vol. 7, No. 4, 1983, pp. 309–320.

[21] Ffowcs Williams, J. E., and Hawkings, D. L., "Sound Generation by Turbulence and Surfaces in Arbitrary Motion," *Philosophical Transactions of the Royal Society of London. Series A, Mathematical and Physical Sciences*, Vol. 264, No. 1151, 1969, pp. 321–342. doi:10.1098/rsta.1969.0031

[22] Kelly, M., and Brown, R., "Influence of Blade Aerodynamic Model on the Prediction of Helicopter High-Frequency Airloads," *Journal of Aircraft*, Vol. 48, No. 2, 2011, pp. 476–494. doi:10.2514/1.C031086